

Measurement of deeply virtual Compton scattering off ${}^4\text{He}$ with the CEBAF Large Acceptance Spectrometer at Jefferson Lab

R. Dupré^{1,21,*} M. Hattawy,^{1,21,33} N. A. Baltzell,^{1,40} S. Bültmann,³³ R. De Vita,¹⁷ A. El Alaoui,^{1,41} L. El Fassi,^{1,27} H. Egryan,⁴⁰ F. X. Girod,⁴⁰ M. Guidal,²¹ K. Hafidi,¹ D. Jenkins,⁴⁷ S. Liuti,⁴⁶ Y. Perrin,²⁵ S. Stepanyan,⁴⁰ B. Torayev,³³ E. Voutier,^{21,25} M. J. Amaryan,³³ W. R. Armstrong,¹ H. Atac,³⁹ C. Ayerbe Gayoso,⁴⁸ L. Barion,¹⁵ M. Battaglieri,^{40,17} I. Bedlinskiy,²⁸ F. Benmokhtar,⁸ A. Bianconi,^{43,20} A. S. Biselli,⁹ M. Bondi,¹⁷ F. Bossù,⁴ S. Boiarinov,⁴⁰ W. J. Briscoe,¹³ D. Bulumulla,³³ V. Burkert,⁴⁰ D. S. Carman,⁴⁰ J. C. Carvajal,¹¹ M. Caudron,²¹ A. Celentano,¹⁷ P. Chatagnon,²¹ V. Chesnokov,³⁷ T. Chetry,^{27,32} G. Ciullo,^{15,10} B. A. Clary,⁶ P. L. Cole,²⁴ M. Contalbrigo,¹⁵ G. Costantini,^{43,20} V. Crede,¹² A. D'Angelo,^{18,36} N. Dashyan,⁴⁹ M. Defurne,⁴ A. Deur,⁴⁰ S. Diehl,^{34,6} C. Djalali,³² M. Ehrhart,^{1,21} L. Elouadrhiri,⁴⁰ P. Eugenio,¹² S. Fegan,⁴⁵ A. Filippi,¹⁹ T. A. Forest,¹⁴ Y. Ghandilyan,⁴⁹ G. P. Gilfoyle,³⁵ R. W. Gothe,³⁸ K. A. Griffioen,⁴⁸ H. Hakobyan,^{41,49} T. B. Hayward,⁴⁸ K. Hicks,³² A. Hobart,²¹ M. Holtrop,²⁹ Y. Ilieva,³⁸ D. G. Ireland,⁴⁴ E. L. Isupov,³⁷ H. S. Jo,²³ K. Joo,⁶ S. Joosten,¹ D. Keller,⁴⁶ G. Khachatryan,⁴⁹ A. Khanal,¹¹ M. Khandaker,³¹ A. Kim,⁶ W. Kim,²³ A. Kripko,³⁴ V. Kubarovsky,⁴⁰ S. E. Kuhn,³³ L. Lanza,¹⁸ K. Livingston,⁴⁴ M. L. Kabir,²⁷ M. Leali,^{43,20} P. Lenisa,^{15,10} I. J. D. MacGregor,⁴⁴ D. Marchand,²¹ N. Markov,^{40,6} V. Mascagna,^{42,20} M. Mayer,³³ B. McKinnon,⁴⁴ M. Mirazita,¹⁶ V. I. Mokeev,⁴⁰ K. Neupane,³⁸ S. Niccolai,²¹ T. R. O'Connell,⁶ M. Osipenko,¹⁷ M. Paolone,^{30,39} L. L. Pappalardo,^{15,10} R. Paremuzyan,^{40,29} E. Paszuk,⁴⁰ D. Payette,³³ W. Phelps,⁵ N. Pivnyuk,²⁸ O. Pogorelko,²⁸ J. Poudel,³³ Y. Prok,³³ M. Ripani,¹⁷ J. Ritman,²² A. Rizzo,^{18,36} G. Rosner,⁴⁴ P. Rossi,^{16,40} J. Rowley,³² F. Sabatié,⁴ C. Salgado,³¹ A. Schmidt,^{13,26} R. Schumacher,³ V. Sergeyeva,²¹ Y. Sharabian,⁴⁰ U. Shrestha,³² D. Sokhan,⁴⁴ O. Soto,^{16,41} N. Sparveris,³⁹ I. I. Strakovsky,¹³ S. Strauch,³⁸ N. Tyler,³⁸ M. Ungaro,^{40,6} L. Venturelli,^{43,20} H. Voskanyan,⁴⁹ A. Vossen,^{7,40} D. Watts,⁴⁵ K. Wei,⁶ X. Wei,⁴⁰ L. B. Weinstein,³³ R. Wishart,⁴⁴ M. H. Wood,² B. Yale,⁴⁸ N. Zachariou,⁴⁵ and J. Zhang⁴⁶
(CLAS Collaboration)

¹Argonne National Laboratory, Argonne, Illinois 60439, USA

²Canisius College, Buffalo, New York 14208, USA

³Carnegie Mellon University, Pittsburgh, Pennsylvania 15213, USA

⁴IRFU, CEA, Université Paris-Saclay, F-91191 Gif-sur-Yvette, France

⁵Christopher Newport University, Newport News, Virginia 23606, USA

⁶University of Connecticut, Storrs, Connecticut 06269, USA

⁷Duke University, Durham, North Carolina 27708-0305, USA

⁸Duquesne University, 600 Forbes Avenue, Pittsburgh, Pennsylvania 15282, USA

⁹Fairfield University, Fairfield, Connecticut 06824, USA

¹⁰Università di Ferrara, 44121 Ferrara, Italy

¹¹Florida International University, Miami, Florida 33199, USA

¹²Florida State University, Tallahassee, Florida 32306, USA

¹³George Washington University, Washington, DC 20052, USA

¹⁴Idaho State University, Pocatello, Idaho 83209, USA

¹⁵INFN, Sezione di Ferrara, 44100 Ferrara, Italy

¹⁶INFN, Laboratori Nazionali di Frascati, 00044 Frascati, Italy

¹⁷INFN, Sezione di Genova, 16146 Genova, Italy

¹⁸INFN, Sezione di Roma Tor Vergata, 00133 Rome, Italy

¹⁹INFN, Sezione di Torino, 10125 Torino, Italy

²⁰INFN, Sezione di Pavia, 27100 Pavia, Italy

²¹Université Paris-Saclay, CNRS/IN2P3, IJCLab, 91405 Orsay, France

²²Institute fur Kernphysik (Juelich), Juelich, Germany

²³Kyungpook National University, Daegu 41566, Republic of Korea

²⁴Lamar University, 4400 M. L. King Boulevard, PO Box 10046, Beaumont, Texas 77710, USA

²⁵LPSC, Université Grenoble-Alpes, CNRS/IN2P3, 38026 Grenoble, France

²⁶Massachusetts Institute of Technology, Cambridge, Massachusetts 02139-4307, USA

²⁷Mississippi State University, Mississippi State, Mississippi 39762-5167, USA

²⁸National Research Centre Kurchatov Institute - ITEP, Moscow 117259, Russia

²⁹University of New Hampshire, Durham, New Hampshire 03824-3568, USA

³⁰New Mexico State University, PO Box 30001, Las Cruces, New Mexico 88003, USA

³¹Norfolk State University, Norfolk, Virginia 23504, USA

*Corresponding author: raphael.dupre@ijclab.in2p3.fr

- ³²*Ohio University, Athens, Ohio 45701, USA*
³³*Old Dominion University, Norfolk, Virginia 23529, USA*
³⁴*II Physikalisches Institut der Universitaet Giessen, 35392 Giessen, Germany*
³⁵*University of Richmond, Richmond, Virginia 23173, USA*
³⁶*Università di Roma Tor Vergata, 00133 Rome, Italy*
³⁷*Skobeltsyn Institute of Nuclear Physics, Lomonosov Moscow State University, 119234 Moscow, Russia*
³⁸*University of South Carolina, Columbia, South Carolina 29208, USA*
³⁹*Temple University, Philadelphia, Pennsylvania 19122, USA*
⁴⁰*Thomas Jefferson National Accelerator Facility, Newport News, Virginia 23606, USA*
⁴¹*Universidad Técnica Federico Santa María, Casilla 110-V Valparaíso, Chile*
⁴²*Università degli Studi dell'Insubria, 22100 Como, Italy*
⁴³*Università degli Studi di Brescia, 25123 Brescia, Italy*
⁴⁴*University of Glasgow, Glasgow G12 8QQ, United Kingdom*
⁴⁵*University of York, York YO10 5DD, United Kingdom*
⁴⁶*University of Virginia, Charlottesville, Virginia 22901, USA*
⁴⁷*Virginia Tech, Blacksburg, Virginia 24061-0435, USA*
⁴⁸*College of William and Mary, Williamsburg, Virginia 23187-8795, USA*
⁴⁹*Yerevan Physics Institute, 375036 Yerevan, Armenia*



(Received 19 February 2021; accepted 6 July 2021; published 11 August 2021)

We report on the measurement of the beam spin asymmetry in the deeply virtual Compton scattering off ${}^4\text{He}$ using the CEBAF Large Acceptance Spectrometer (CLAS) at Jefferson Lab using a 6 GeV longitudinally polarized electron beam incident on a pressurized ${}^4\text{He}$ gaseous target. We detail the method used to ensure the exclusivity of the measured reactions, in particular the upgrade of CLAS with a radial time projection chamber to detect the low-energy recoiling ${}^4\text{He}$ nuclei and an inner calorimeter to extend the photon detection acceptance at forward angles. Our results confirm the theoretically predicted enhancement of the coherent ($e {}^4\text{He} \rightarrow e' {}^4\text{He}' \gamma'$) beam spin asymmetries compared to those observed on the free proton, while the incoherent ($e {}^4\text{He} \rightarrow e' p' \gamma' X$) asymmetries exhibit a 30% suppression. From the coherent data, we were able to extract, in a model-independent way, the real and imaginary parts of the only ${}^4\text{He}$ Compton form factor, \mathcal{H}_A , leading the way toward 3D imaging of the partonic structure of nuclei.

DOI: [10.1103/PhysRevC.104.025203](https://doi.org/10.1103/PhysRevC.104.025203)

I. INTRODUCTION

In the past few decades, the study of the proton structure has made significant progress thanks to the theoretical and experimental developments of three-dimensional structure functions [1]. These studies, which have focused on generalized parton distributions (GPDs) and transverse momentum dependent parton distribution functions (TMDs), can be generalized to the nucleus and offer a unique opportunity to revisit the quark structure of the nucleus with an original perspective [2]. This new approach is particularly needed as the quark structure of the nucleus remains today the subject of numerous controversies. Indeed, while much progress has been made in measuring the nuclear parton distribution functions, their shape can be explained with very different model assumptions [3–5].

In nuclei, the GPDs can be probed conveniently through the measurement of the spin asymmetries generated by the deeply virtual Compton scattering (DVCS) process [6–9]. The measurement of the exclusive production of a photon limits the possibilities of final-state interactions (FSIs) in the nuclear medium and offers a unique opportunity to make a measurement free of them. Moreover, with a spin-0 nuclear target, the extraction of the GPD from the DVCS data is

significantly simplified since a single GPD is involved in the process at leading order. However, the measurement of the nuclear DVCS is challenging experimentally and the first attempts by the HERMES Collaboration [10] to unravel an A -dependent nuclear effect have been unsuccessful. We present here in detail the more recent measurements by the CLAS Collaboration, which has been already partially presented in two short Letters [11,12]. We extend in this article the description of the CEBAF Large Acceptance Spectrometer (CLAS) nuclear DVCS experiment, detail the methods used for the data analysis, and produce the complete experimental results for each channel measured.

II. THEORETICAL FRAMEWORK

A. The GPD formalism

The theory of GPDs has been already reviewed in detail in various publications [6–9], and we summarize here only the necessary elements to discuss the present experimental results. The GPDs are real structure functions $F^q(x, \xi, t)$, where $x + \xi$ and $x - \xi$ are the incoming and outgoing quark momenta, respectively, and $t = \Delta^2$ is the squared transferred 4-momentum to the target, as illustrated in Fig. 1.

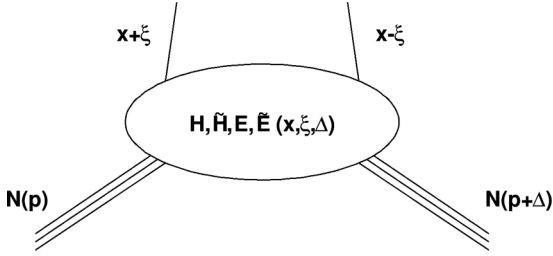


FIG. 1. General representation for the GPDs of a nucleon represented by the triple lines and noted N . Single lines can represent quarks or antiquarks probed in the nucleon shown by the triple lines.

The different possible spin states lead to several independent GPDs for any given hadron. The proper accounting of the number of GPDs must be done with regard to the symmetries of the system. At leading order and leading twist, we find that there are $2(2J + 1)^2$ GPDs for a particle of spin J . Therefore for a spin-0 hadron like the ${}^4\text{He}$ nucleus, we will have two GPDs, and for a spin-1/2 hadron like the proton, eight GPDs. Half of these involve a parton helicity flip; they are called transversity GPDs and do not contribute to the DVCS process.

DVCS is the main experimental probe of the GPDs. However, this process does not allow for an extraction of the GPDs in the full phase space of the parameters. Instead, DVCS gives access to the GPDs integrated over x . To account for this and simplify the notation, we define the complex Compton form factors (CFFs; noted with curved \mathcal{F} for a given GPD F) for each GPD as follows:

$$\text{Re}[\mathcal{F}(\xi, t)] = \sum_q e_q^2 \mathcal{P} \int_{-1}^1 dx F^q(x, \xi, t) \left[\frac{1}{x - \xi} \mp \frac{1}{x + \xi} \right], \quad (1)$$

$$\text{Im}[\mathcal{F}(\xi, t)] = -\pi \sum_q e_q^2 [F^q(\xi, \xi, t) \mp F^q(-\xi, \xi, t)]. \quad (2)$$

These are the quantities directly present in the DVCS cross sections. We note that they are summed over the different

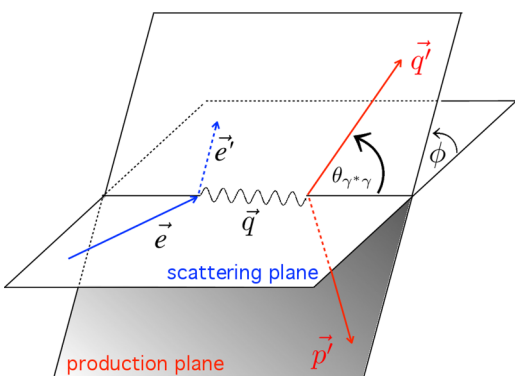


FIG. 2. Illustration of the scattering (or leptonic) and production (or hadronic) planes in the DVCS process.

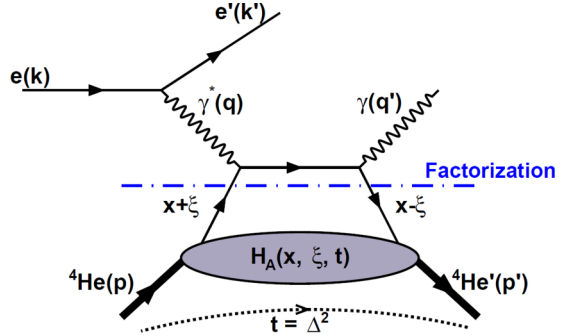


FIG. 3. Diagram representing the coherent nuclear DVCS, where we indicate the limit between the hard and the soft components with the dot-dashed factorization line.

quark flavors present in the hadron, as the electromagnetic probe does not differentiate quark flavors.

Experimentally, another process is indistinguishable from DVCS, the Bethe-Heitler (BH) process in which the final-state photon is emitted by the scattering lepton rather than the hadron. In this case, the photon-hadron interaction is the same as in elastic scattering and depends on the target form factors rather than its GPDs. The DVCS and BH processes are experimentally indistinguishable as they have identical final states, such that they interfere in the squared amplitude of the exclusive photoproduction process:

$$|T|^2 = |T_{\text{DVCS}}|^2 + |T_{\text{BH}}|^2 + T_{\text{DVCS}}^* T_{\text{BH}} + T_{\text{DVCS}} T_{\text{BH}}^*. \quad (3)$$

The interference terms significantly increase the cross section in specific parts of the phase space and lead to significant beam spin asymmetries (BSAs), which are the focus of the measurements presented here.

Finally, we need to define the kinematics. We use the conventions from Fig. 2 for angles and the experimental kinematic variables used here are defined as $-t = -(p_p - p'_p)^2 = \Delta^2$ and $x_B = \frac{Q^2}{2M_N v} \sim \frac{2\xi}{1+\xi}$, with M_N the nucleon mass and v the energy transfer to the target, $v = E - E'$.

B. Coherent nuclear DVCS

The first reaction measured in the experiment is the coherent electroproduction of a photon on helium $e + {}^4\text{He} \rightarrow e' + \gamma + {}^4\text{He}'$ at large 4-momentum transfer squared (Q^2). The leading order diagram of the nuclear coherent DVCS is represented in Fig. 3. In the present experiment, we focused on the measurement of the BSA noted A_{LU} with L for the longitudinally polarized electron beam and U the unpolarized target, which is defined as

$$A_{LU} = \frac{d^5\sigma^+ - d^5\sigma^-}{d^5\sigma^+ + d^5\sigma^-}, \quad (4)$$

where $d^5\sigma^+$ ($d^5\sigma^-$) is the differential cross section for a positive (negative) beam helicity. At leading order and leading

twist, the BSA can be expressed as [13]

$$A_{LU} = \frac{x_A(1+\epsilon^2)^2}{y} s_1^{\text{INT}} \sin(\phi) \left/ \left[\sum_{n=0}^{n=2} c_n^{\text{BH}} \cos(n\phi) + \frac{x_A^2 t(1+\epsilon^2)^2}{Q^2} P_1(\phi) P_2(\phi) c_0^{\text{DVCS}} + \frac{x_A(1+\epsilon^2)^2}{y} \sum_{n=0}^{n=1} c_n^{\text{INT}} \cos(n\phi) \right] \right], \quad (5)$$

where $P_1(\phi)$ and $P_2(\phi)$ are the BH propagators, and $x_A = \frac{M_p \cdot x}{M_{^4\text{He}}}$. The factors $c_{0,1,2}^{\text{BH}}$, c_0^{DVCS} , $c_{0,1}^{\text{INT}}$, and s_1^{INT} are the Fourier coefficients of the BH, the DVCS, and the interference amplitudes for a spin-zero target, respectively. The explicit expressions of these coefficients, which have been derived based on the work of Kirchner and Müller [13], can be found in Appendix A.

This formula can be expressed in a simplified manner for a spin-0 target as [14]

$$A_{LU}(\phi) = \frac{\alpha_0(\phi) \text{Im}(\mathcal{H}_A)}{\alpha_1(\phi) + \alpha_2(\phi) \text{Re}(\mathcal{H}_A) + \alpha_3(\phi) [\text{Re}(\mathcal{H}_A)^2 + \text{Im}(\mathcal{H}_A)^2]}, \quad (6)$$

where $\text{Im}(\mathcal{H}_A)$ and $\text{Re}(\mathcal{H}_A)$ are the imaginary and real parts, respectively, of the CFF \mathcal{H}_A associated with the GPD H_A of the spin-0 nucleus. The α_i factors are ϕ -dependent kinematical terms that depend on the nuclear form factor F_A and the independent variables Q^2 , x , and t . These factors have the following simplified expressions:

$$\alpha_0(\phi) = \frac{x_A(1+\epsilon^2)^2}{y} S_{++}(1) \sin(\phi), \quad (7)$$

$$\alpha_1(\phi) = c_0^{\text{BH}} + c_1^{\text{BH}} \cos(\phi) + c_2^{\text{BH}} \cos(2\phi), \quad (8)$$

$$\alpha_2(\phi) = \frac{x_A(1+\epsilon^2)^2}{y} [C_{++}(0) + C_{++}(1) \cos(\phi)], \quad (9)$$

$$\alpha_3(\phi) = \frac{x_A^2 t(1+\epsilon^2)^2}{y} \mathcal{P}_1(\phi) \mathcal{P}_2(\phi) \cdot 2 \frac{2 - 2y + y^2 + \frac{\epsilon^2}{2} y^2}{1 + \epsilon^2}, \quad (10)$$

where $S_{++}(1)$, $C_{++}(0)$, and $C_{++}(1)$ are the Fourier harmonics found in the leptonic tensor [14]. Their explicit expression are provided in Appendix A.

Equation (6) is particularly convenient to perform an extraction of $\text{Im}(\mathcal{H}_A)$ and $\text{Re}(\mathcal{H}_A)$ through a fit of the BSA as a function of ϕ . As can be seen in Fig. 4, the form of each α coefficient has a characteristic ϕ dependence, such that a fit can easily separate their respective contributions. The only caveat is the large difference of magnitude between the α factors, which can lead to rather different error propagation for the two parts of the CFF.

An important issue with the use of this theoretical framework is the large mass of the helium nucleus. Recent work indicates that the effect of this correction is moderate [15];

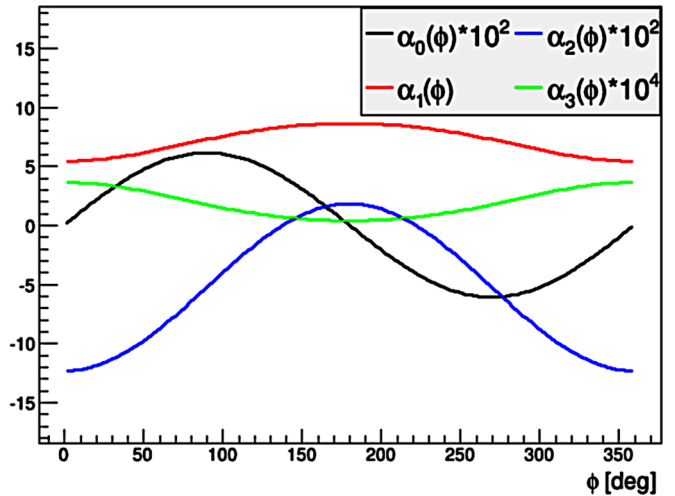


FIG. 4. Coefficients presented in Eqs. (7) to (10). Note the prescaling factors used for α_0 , α_2 , and α_3 .

however the applicability to such a large mass remains to be fully explored from the theoretical point of view.

C. Incoherent nuclear DVCS

The incoherent nuclear DVCS process is the DVCS off a bound nucleon in a nucleus as represented in Fig. 5 for a ${}^4\text{He}$ target. The remnants of the nucleus (X) contain only the missing three nucleons. The theory for incoherent DVCS on the nucleon is largely based on the free-proton theory already reviewed widely in the literature [6,7,9]. Two important differences need to be accounted for however: the different initial state and the addition of FSIs. In the initial state, the intrinsic Fermi motion of the nucleons in the nucleus leads to an uncertainty on the exact kinematics of the reaction. Moreover, in general, the nucleon is in an off-shell state that is not exactly identical to its final state. In the final state, interactions between the outgoing nucleon from the DVCS reaction and the remnants of the nuclear target are possible. The latter leads to contamination from other channels; in particular, charge

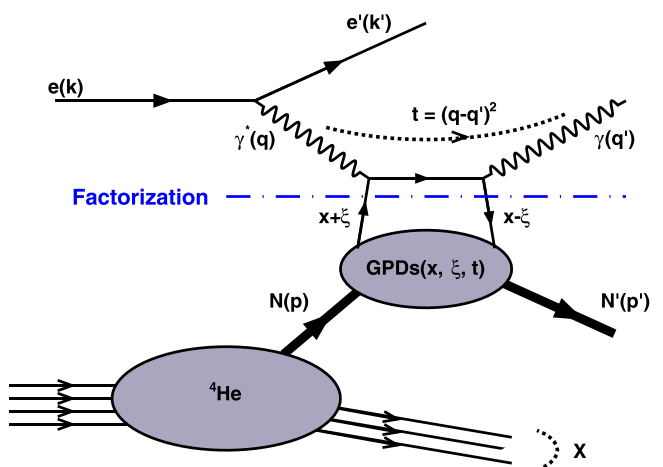


FIG. 5. Diagram representing the incoherent nuclear DVCS.

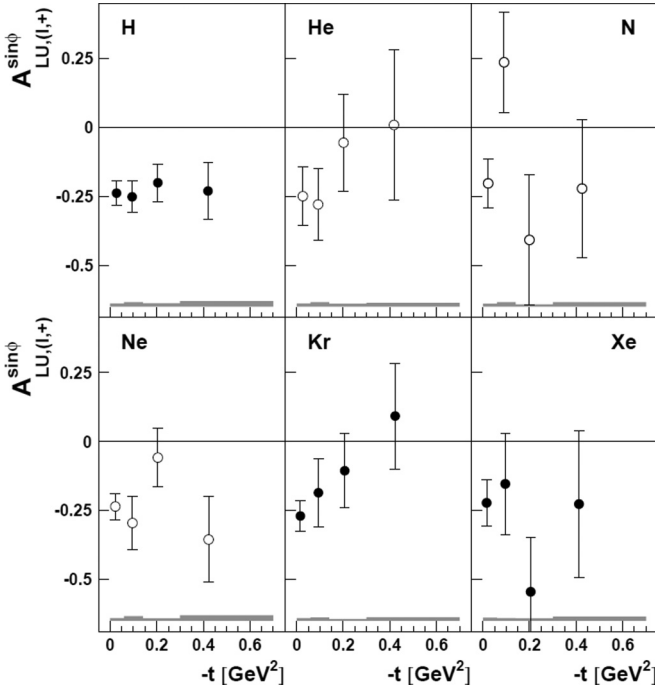


FIG. 6. The $\sin(\phi)$ moment of the BSA as a function of $-t$ measured by HERMES for a series of nuclei [10]. The gray bands represent the systematic uncertainties.

exchange processes can lead to a large contribution from such background reactions.

Since DVCS is a process selected using tight exclusivity constraints, some of the initial- and final-state effects are automatically mitigated. Selection criterion on missing energy and momentum are performed, constraining the range of initial Fermi motion and FSIs possible. However, no theoretical calculation is available to correct for the remainder of these effects yet. Modern calculations exist for such effects in deep inelastic scattering [16] and quasielastic scattering [17], and we can expect them to be extended to the DVCS process as more data become available. Another avenue of progress on this topic will be the use of experimental techniques like tagging. This process can help to control both initial- and final-state effects by detecting the nuclear remnant. In the tagged process the target breaks in two; thus measuring the nuclear remnant provides information about the initial state of the struck nucleon, while a backward fragment also limits significantly the probability of FSIs.

III. PAST NUCLEAR DVCS MEASUREMENTS

The first measurement of nuclear DVCS was performed by the HERMES Collaboration [10]. This experiment covered an array of nuclear targets and looked at the A dependence of the BSA signal. Their main results, reproduced in Figs. 6 and 7, suffer from large uncertainties, which makes them consistent with the free-proton data and prevents us from reaching strong conclusions about possible nuclear effects. Yet, in the coherent DVCS case a rather strong effect was expected, leading

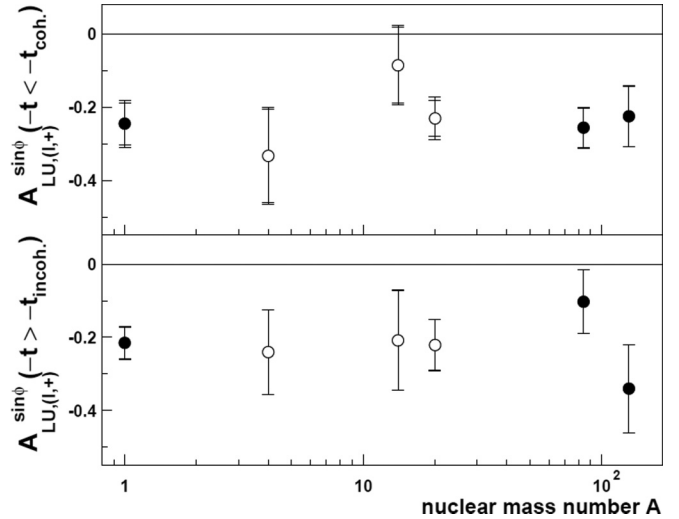


FIG. 7. The $\sin(\phi)$ moment of the BSA at low and high $-t$ as a function of A measured by HERMES [10]. The inner error bars represent the statistical uncertainty, while the outer represent the quadratic sum of the statistical and systematic uncertainties.

to an apparent conflict between the HERMES results and theoretical expectations.

A characteristic of the HERMES measurement and how it was obtained from data can however explain the discrepancy with theoretical expectations [10,18], the main point being that the DVCS process is not fully detected and the scattered target is instead reconstructed through a missing mass measurement of the other reaction products. The issue with this method is that the detector resolution is not good enough to separate the coherent and incoherent channels properly. Thus, the results are labeled “coherent enriched” and “incoherent enriched” at low and high $-t$, respectively. This label is based on the assumption that the very different behavior of the cross sections of the two channels in t will lead to a clear differentiation. However, the results in Fig. 7 show similar behaviors in both sectors of t , which challenges this assumption and could explain the tension between theory and experiment.

Altogether, large error bars and the impossibility to properly separate the coherent and incoherent channels have strongly impaired the interpretation of the measurement and the conclusions that can be obtained from it. The CLAS experiment presented here has profited largely from this result and was designed specifically to solve these two issues of low statistics and exclusivity.

IV. THE CLAS NUCLEAR DVCS EXPERIMENTAL SETUP

The CLAS nuclear DVCS experiment had as its main objectives to explore coherent DVCS on ${}^4\text{He}$, to assess whether the predicted BSA increase could be observed, and to extract the ${}^4\text{He}$ GPD. In order to perform this measurement however, several instrumentation challenges needed to be resolved. First, to measure the scattered electron and the small-angle photon from DVCS, we used CLAS in its DVCS setup, i.e., with the addition of a forward-angle calorimeter and a 5-T solenoid magnet. Second, a radial time projection chamber

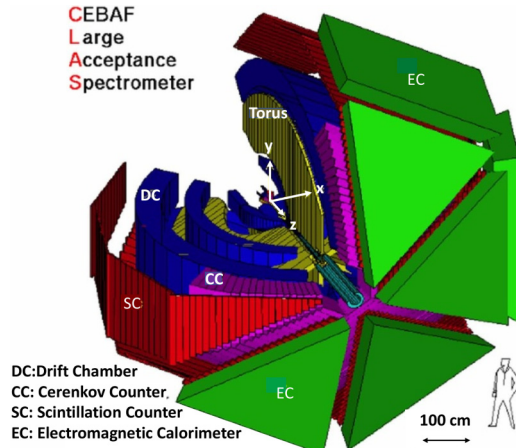


FIG. 8. View of the CLAS detector setup.

(RTPC) was installed to measure the helium recoils and thus ensure the exclusivity of the process in the coherent channel. In this section, we will review the important elements of this detection setup.

A. The CEBAF Large Acceptance Spectrometer

The CLAS [19] spectrometer was installed in Hall B of the Jefferson Lab (JLab) continuous electron beam accelerator facility (CEBAF). This detector was specifically designed to study the multiparticle final states that cannot be observed conveniently with multiarm spectrometers. It was naturally well suited for measuring DVCS, and several DVCS experiments were successfully conducted before this experiment using multiple different configurations. CLAS was composed of six identical sectors separated by the coils of a toroidal magnet, with each sector made of four detectors as shown in Fig. 8. Three regions of drift chambers [20] were placed between the torus magnet to reconstruct the charged particles' tracks and calculate their momentum. An array of scintillators was placed behind the drift chambers to measure the precise time of flight for each track [21]. These detectors covered the polar angle from 8 to 142 degrees. In the forward region, from 8 to 45 degrees, these detectors were complemented with Cerenkov counters [22] and electromagnetic calorimeters [23], important for electron identification and photon detection.

Altogether, CLAS provided a large acceptance for momenta starting at 200 MeV. The nuclear DVCS experiment took place from October to December 2009 at an electron beam energy of 6.064 GeV, with the beam intensity varying between 120 and 150 nA. This beam, on the ${}^4\text{He}$ target pressurized between 5 and 6 atm, corresponds to luminosities in the range of 1 to $1.2 \times 10^{34} \text{ cm}^{-2} \text{ s}^{-1}$. During the experiment, the data acquisition operated at a rate of about 3 kHz with about 70% live time using an inclusive electron trigger.

B. Adaptations for DVCS

The CLAS Collaboration has established a specific setup to measure the typically small-angle photons of the DVCS

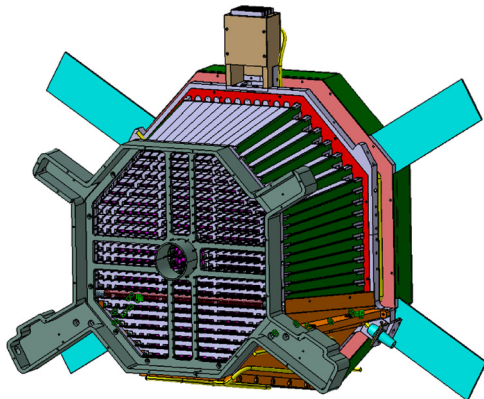


FIG. 9. Representation of the inner calorimeter (IC) of CLAS. The crystals that compose the sensitive part of the detector are represented in purple.

process. This setup is composed of an inner calorimeter and a solenoid and has been employed for numerous DVCS measurements on proton targets [24–26].

The inner calorimeter, illustrated in Fig. 9, is a homogeneous calorimeter composed of 424 lead tungstate (PbWO) crystals read out by $5 \times 5 \text{ mm}^2$ avalanche photodiodes (APDs). It covers angles from 4 to 15 degrees. However, placing a detector at such small angles makes it particularly sensitive to the low-energy Møller electrons scattered from the target. To protect the calorimeter from this background, a 5-T solenoid was placed around the target to form a magnetic shield. Thanks to this field, low-energy charged particles (particularly electrons) curled around the beamline and never made it to the calorimeter or other CLAS detectors as illustrated by the simulation results presented in Fig. 10. This allows us to run much higher luminosity experiments, a necessity for low-rate processes like DVCS.

C. The radial time projection chamber

The recoil helium nuclei from coherent DVCS are mostly emitted between 150 and 200 MeV at the beam energy of 6 GeV. Therefore, a specific detector was needed to detect them. To design the present setup, inspiration was drawn from the BONUS setup that also used a GEM-based RTPC [27] in CLAS to detect slow protons coming out of a deuterium

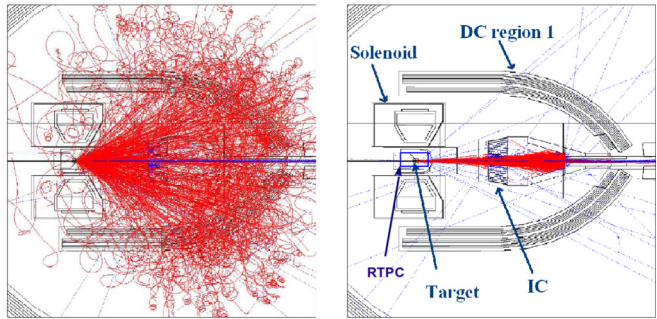


FIG. 10. Representation of the center of CLAS with the beam background in red with and without the solenoid field activated, right and left, respectively.

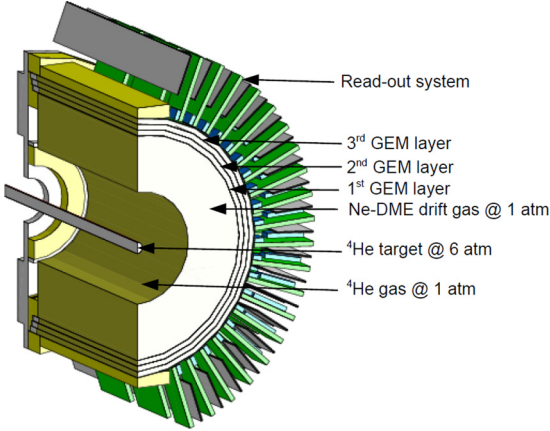


FIG. 11. Cut view of the RTPC.

target [28]. In such an RTPC the ionization electrons drift toward large radii rather than toward the end caps, as is more traditional in time projection chambers. This design allows us to reduce significantly the drift time and reduce the amount of pileup from accidental events. The RTPC design, its operation and calibration, and the track reconstruction have been described in more detail elsewhere [29]. Here a summary of key elements is provided.

In order to detect the recoil helium nuclei from a DVCS reaction, we first need to ensure that it will come out of the target. For this, we used a light straw target made of a thin Kapton wall of $27 \mu\text{m}$ filled with helium at 6 atm pressure. The entrance and exit windows are thin aluminum foils and a helium bag was placed downstream of the target to avoid interaction with air in the gap between the target and the beamline vacuum. The cylindrical chamber surrounds the target as illustrated in Fig. 11. Here we list the elements composing it based on their radii:

- (i) Up to a radius of 3 mm the pressurized helium target.
- (ii) From 3 to 20 mm a keep-out zone filled with 1 atm of helium to minimize the production of secondaries.
- (iii) At 20 mm a grounded foil made of $4 \mu\text{m}$ aluminized Mylar to isolate the chamber from the beamline region and collect charges. It also serves to separate the gas regions.
- (iv) From 20 to 30 mm a dead zone filled with the drift gas to separate the ground from the cathode.
- (v) At 30 mm the cathode foil made of $4 \mu\text{m}$ aluminized Mylar.
- (vi) From 30 to 60 mm the drift region filled with the drift gas, a mix of neon and dimethyl ether (DME) in an 80/20 proportion.
- (vii) From 60 to 69 mm the amplification regions, filled with drift gas, with GEM foils placed at 60, 63, and 66 mm.
- (viii) At 69 mm the collection pads connected to the preamplifiers placed directly outside the chamber.

The time-to-position calibration of the detector has been performed with a dependence on z , the position along the beamline axis, due to variations in the magnetic fields. To per-

form this calibration we took dedicated data at 1.2 GeV beam energy. In this data set, we were able to select elastic events, for which the kinematics of the helium recoil can be calculated from the electron kinematics and directly compared to the measurement in the RTPC. This comparison helped to map the correspondence between time and position in the chamber and determine the drift path of electrons. A more detailed description of the calibration process is available in Ref. [29].

V. DVCS EVENT SELECTION

A. Particle identification

The scattered electrons were detected with the baseline CLAS detectors. The drift chamber measured the kinematics of the electron and the signal measured in both the Cerenkov counter and electromagnetic calorimeter provided the identification. A signal of good quality was also required in the time-of-flight system, which served as a time reference for all detectors. Protons were detected with the baseline CLAS detectors as well, the drift chamber measured the kinematics of the proton, and the time-of-flight system ensured its identification. Several fiducial cuts are applied to ensure that particles did not go through part of the inner calorimeter or the solenoid, as well as to reject the edges of the detectors, where their efficiency is rapidly decreasing. Kinematic corrections are also applied to the electrons and protons to correct for energy loss and biases in calibration, which are at the subpercent level except for protons below 500 MeV for which they go up to 10% at the detection limit of 200 MeV.

The photons from DVCS are mainly detected with the inner calorimeter. No specific identification cuts were used in this detector as large energy deposit was dominantly from electrons and photons, which could not be separated reliably. However, the detection of an electron at large angle in CLAS highly suppressed the number of electrons in the calorimeter; moreover, the exclusivity cuts used later in the analysis further this suppression. Leftover accidentals were accounted for in the background subtraction described below. The inner calorimeter was calibrated through a series of steps, involving the reconstruction of π^0 from their decay into two photons. Calibration was obtained with an iterative process to adjust each crystal gain to obtain the most accurate π^0 mass. A global calibration of the calorimeter was also performed to account for incident angle, energy, and time-dependent effects.

The ${}^4\text{He}$ nuclei were detected with the RTPC using a series of constraints on the quality of the track reconstruction. As the chamber was operated at low gain and had very low efficiency for protons, we did not apply further identification cuts for the ${}^4\text{He}$ nuclei detection [29].

Finally, we selected events that contain a single electron, a high-energy photon ($E > 2 \text{ GeV}$), and either a helium or a proton. We applied a selection cut on the two charged particles to ensure that they originated from the same vertex inside the target, thus rejecting accidentals and events from the target windows. Moreover, since we are aiming to study deep processes occurring at the partonic level, we selected $Q^2 > 1 \text{ GeV}^2$. Also, the transferred momentum squared to the recoil ${}^4\text{He}$ was bound by a minimum value based on basic

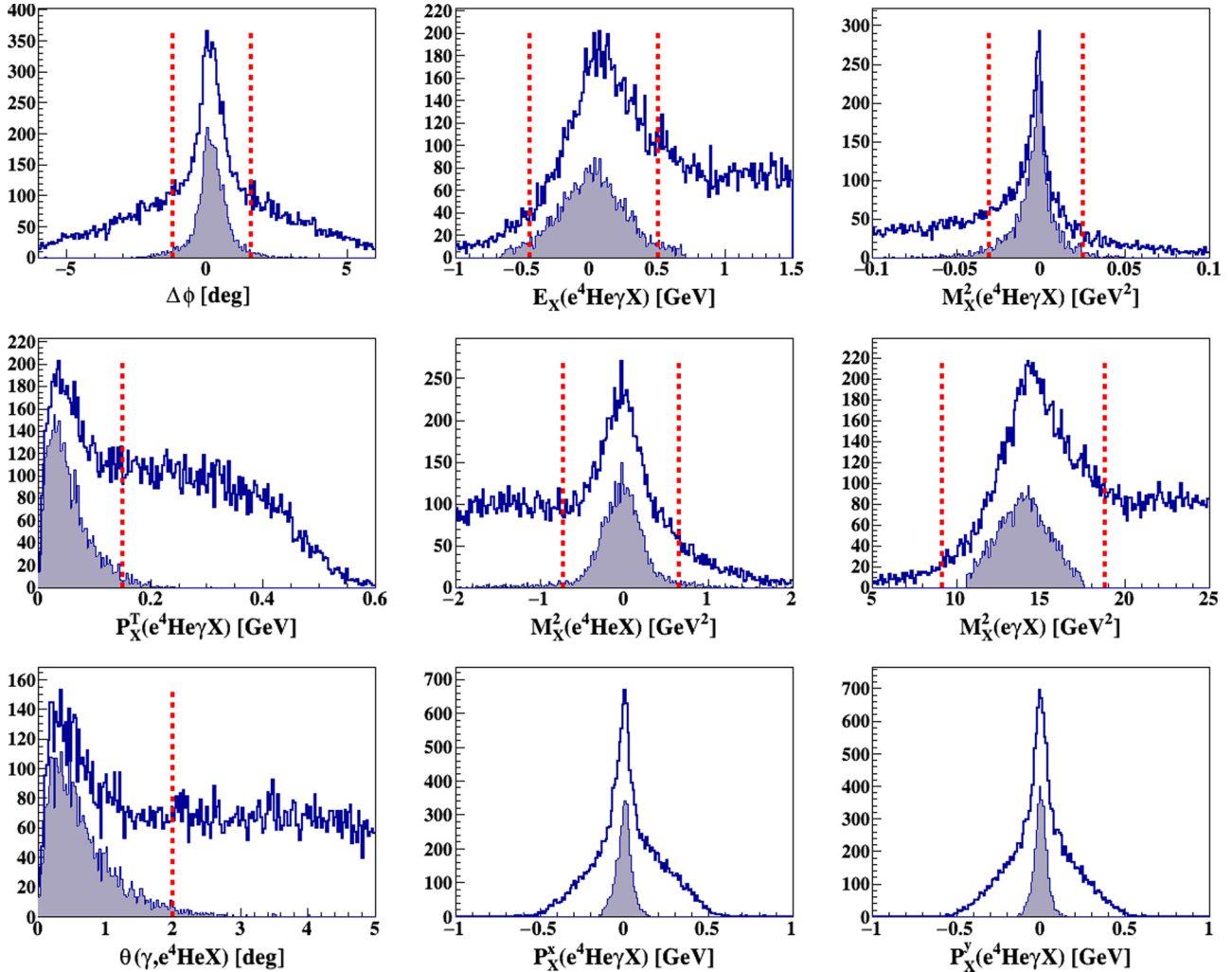


FIG. 12. Distributions of the coherent photon production events before (blue) and after (black line filled in gray) the exclusivity cuts used to select coherent DVCS represented by the red dashed lines. The histograms are shown as a function of the seven variables used for the exclusivity selection described in the text, plus the missing P_x and P_y components, in order left to right and top to bottom.

energy-momentum conservation:

$$t_{\min} = -Q^2 \frac{2(1-x_A)(1-\sqrt{1+\epsilon^2}) + \epsilon^2}{4x_A(1-x_A) + \epsilon^2}, \quad (11)$$

where $\epsilon^2 = \frac{4M_{^4\text{He}}^2 x_A^2}{Q^2}$. For incoherent DVCS, we used a similar cut where x_A is replaced by x and $M_{^4\text{He}}$ by M_p .

B. Exclusive photoproduction selection

In principle, a selection based only on the missing energy of the system would be enough to guarantee the exclusivity of the process. However, in our experiment, where particles were detected at very different energies and with very different detector resolutions, this method was not sufficient. For instance the momentum of the helium nuclei is negligible in the missing energy observable; thus this valuable information has no impact on a selection using this observable only. To address this issue, we constrained the selection of our exclusive events by using seven variables selected to optimize the use

of all the detector information available. The seven variables are defined as follows for the coherent DVCS case (replace helium by proton for the incoherent case):

- (i) Co-planarity ($\Delta\phi$) of the virtual photon, the real photon, and the recoil helium.
- (ii) Missing energy of the complete final state.
- (iii) Missing mass of the complete final state.
- (iv) Missing transverse momentum of the complete final state.
- (v) Missing mass of the electron-helium system.
- (vi) Missing mass of the electron-photon system.
- (vii) Collinearity (θ) of the measured photon with the missing momentum of the electron-helium system.

In the analysis, we applied selection cuts based on a fit of the exclusive peak at 3σ around the mean value for each variable. This systematic method helps to avoid any bias in the selection of the events. The selection of coherent DVCS with these variables is illustrated in Fig. 12. We note on these dis-

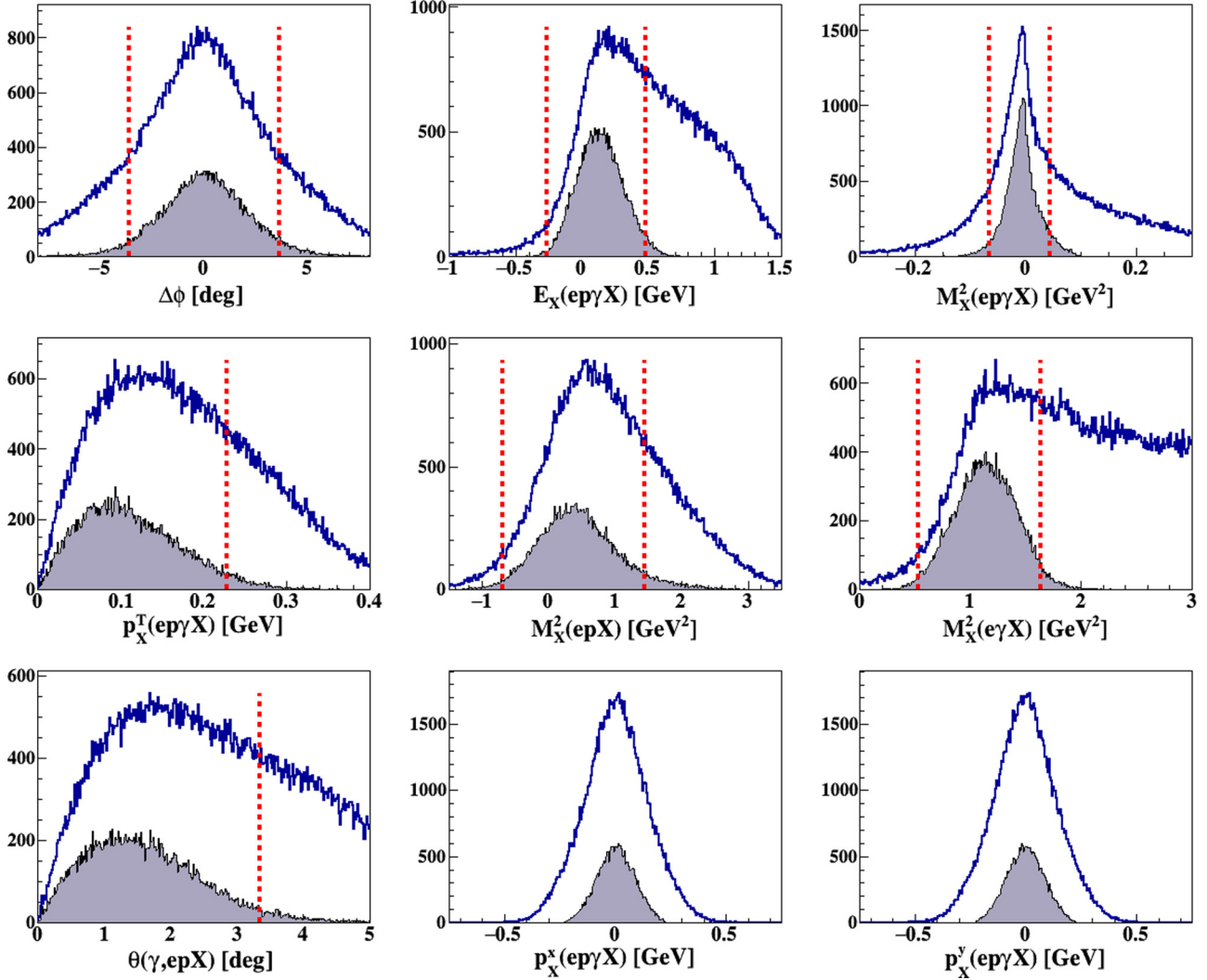


FIG. 13. Distributions of the incoherent photon production events before (blue) and after (black line filled in gray) the exclusivity cuts used to select coherent DVCS represented by the red dashed lines. The histograms are shown as a function of the seven variables used for the exclusivity selection described in the text, plus the missing P_x and P_y components, in order left to right and top to bottom.

tributions only a few minor anomalies, where the distributions have some asymmetries. These are linked with the detector resolution, which impacts some of the kinematic variables nonlinearly. The selection of incoherent DVCS is presented in Fig. 13, with two main differences: wider distributions and larger offset from the nominal expectations. The wider distributions are mainly attributed to the effect of Fermi motion, but simulations have shown that this effect is not strong enough to fully reproduce the distribution widths and FSIs must play a role as well. The offsets of some distributions are caused by slight detector misalignment between CLAS sectors and are within the levels obtained with free-proton targets [26] to which they can be directly compared.

C. Background subtraction

The main signal contamination comes from the exclusive production of a π^0 , the final state of which is very similar to DVCS with only an extra photon. In such an event, if one of

the photons is produced at low energy, it is easy to confuse this process with single-photon production. In order to estimate the contribution from this channel in the data, we measured the exclusive π^0 production in the same way as DVCS, with a series of exclusivity cuts, completed by a selection cut on the invariant mass of the two photons to match the π^0 mass. The events obtained for the coherent and incoherent channels are shown in Figs. 14 and 15, respectively. Using this sample, we developed an event generator and adjusted it to the data, the result of which is shown with the red histograms of Figs. 14 and 15. To correct the experimental data, we then estimated the number of single-photon events coming from the exclusive π^0 production as

$$N_{1\gamma,\pi^0}^{\text{Exp}} = \frac{N_{1\gamma,\pi^0}^{\text{Sim}}}{N_{2\gamma,\pi^0}^{\text{Sim}}} \times N_{2\gamma,\pi^0}^{\text{Exp}}, \quad (12)$$

where $N_{1\gamma,\pi^0}^{\text{Sim}}$ is the number of simulated exclusive π^0 mistaken for DVCS events, $N_{2\gamma,\pi^0}^{\text{Sim}}$ the number of simulated

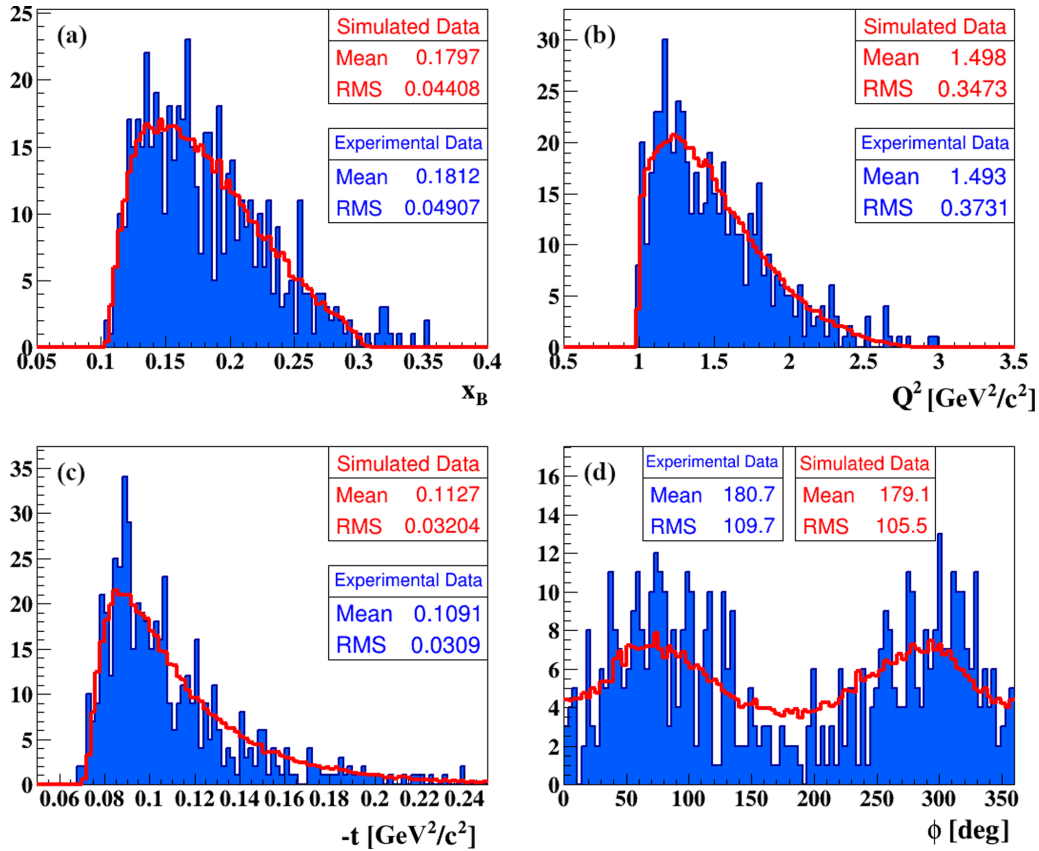


FIG. 14. The measured (filled blue) and simulated (red) distributions of coherent exclusive π^0 production as a function of x (a), Q^2 (b), $-t$ (c), and ϕ (d).

exclusive π^0 fully reconstructed, and $N_{2\gamma,\pi^0}^{\text{Exp}}$ the number of experimentally measured exclusive π^0 . This number was then subtracted from the experimentally measured number of DVCS events ($N_{\text{DVCS}}^{\text{Exp}}$) to get the corrected result:

$$N_{\text{DVCS}}^{\text{Corr}} = N_{\text{DVCS}}^{\text{Exp}} - N_{1\gamma,\pi^0}^{\text{Exp}}. \quad (13)$$

We show in Fig. 16 the π^0 contamination for the $-t$ bins, where it varies the most from one bin to another. The study shows 2% to 4% contamination in the coherent channel and 3% to 17% in the incoherent channel. After subtracting this contamination from the denominator of the asymmetry, we make no further correction to the DVCS BSA; i.e., we assume the exclusive π^0 production has no such asymmetry in either the coherent or incoherent channels. Our own exclusive π^0 data rule out any BSA above approximately 10%, a level which would have an insignificant effect on our results given the small amount of contamination.

The second important source of background comes from accidentals. Despite the many exclusivity cuts, it is possible to have particles from different events being combined and pass all the cuts to get into the data sample. To evaluate the number of such events, we inverted the vertex selection of the two charged particles of the process, electron and helium (or proton in the incoherent case), and requested that they be separate. We found that 4.1% of the coherent and 6.5% of the

incoherent samples were accidentals; they are also subtracted from the denominator of the asymmetry.

D. Systematic uncertainties

To further evaluate the systematic uncertainty of the measurements, we performed several specialized studies. We evaluated the impact of changing the exclusivity selection cuts by varying them from 1 to 5σ . We also evaluated the impact of changing the binning in ϕ on the extraction of the BSA at 90 degrees. The beam polarization was measured using Møller scattering runs; the uncertainty was estimated based on the known precision of the dedicated apparatus and the spread of the measurements during the complete run period. We studied how different methods of simulating the exclusive π^0 production affected the single-photon background and further estimated how much bias could arise from an undetected BSA in the process. As radiative corrections are expected to be small for this process, we did not apply them, but associated an uncertainty equal to their expected value. These uncertainties are summarized in Table I, with their respective evaluated values. They are added quadratically to obtain the total systematic uncertainty presented in the results.

An extra problem that was studied is the best way to define t in the incoherent channel, which is not completely straightforward. As can be seen in Fig. 5, we can either use t or $t' [= (p - p')^2]$. In principle, the two are identical, but

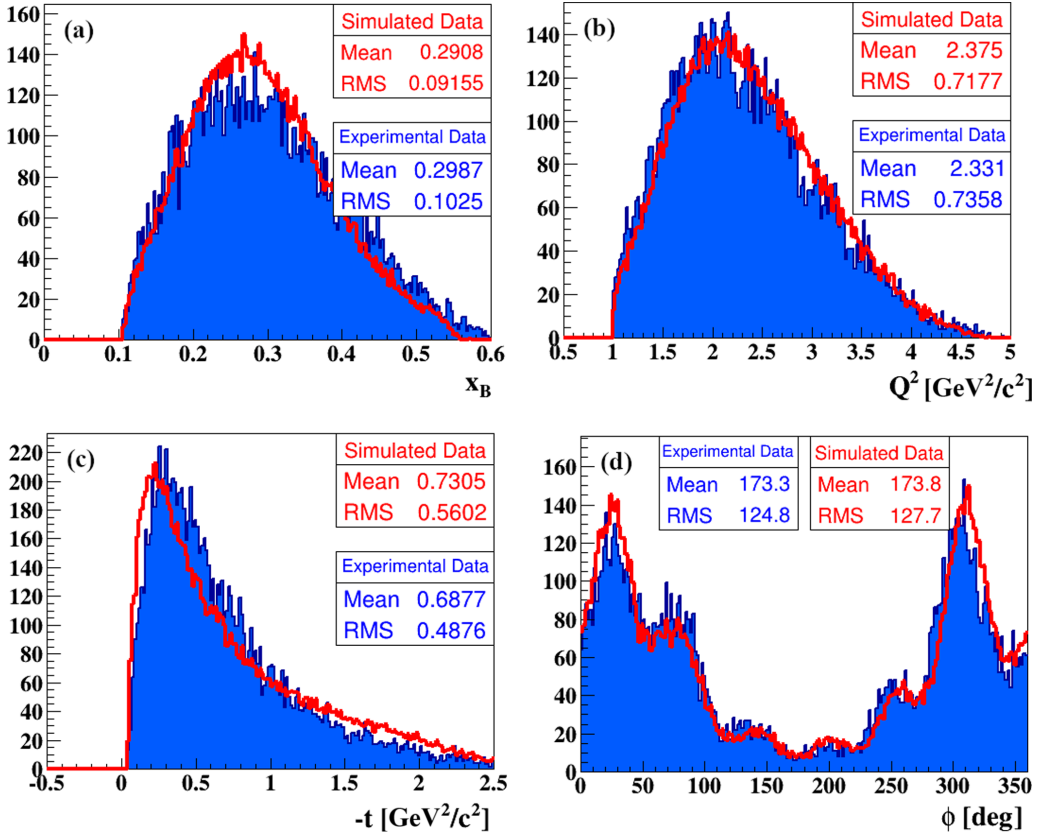


FIG. 15. The measured (filled blue) and simulated (red) distributions of incoherent exclusive π^0 production as a function of x (a), Q^2 (b), $-t$ (c), and ϕ (d).

experimentally we face some issues. The measurement of t is less precise than t' because it involves the photon rather than charged particles. However, the exact measurement of t' is impossible and one needs to assume a proton at rest in the initial state to calculate t' . As it is not obvious which solution is best, we studied the difference between the two results by analyzing the data independently using the two definitions. We found no significant difference between them, as is illustrated in Fig. 17. We use in the final results t as it is based on the rigorous definition. Since the effect of resolution appears small and is partly accounted for in the systematic uncertainty associated with the DVCS cuts, we decided not to associate an extra systematic uncertainty based on this study.

VI. RESULTS

A. Coherent DVCS

In Fig. 18, we present the results for the BSA in the coherent DVCS channel. We observe the dominant sinusoidal component typical of the DVCS BSA, with an amplitude almost double that measured for the free proton [25]. This predicted feature of nuclear DVCS [18] is observed here for the first time, due to the fact that this measurement cleanly isolates the coherent DVCS process. The absence of this feature in the previous measurement by HERMES [10] and its clear observation here indicates that the recoil detection is necessary to isolate the effects

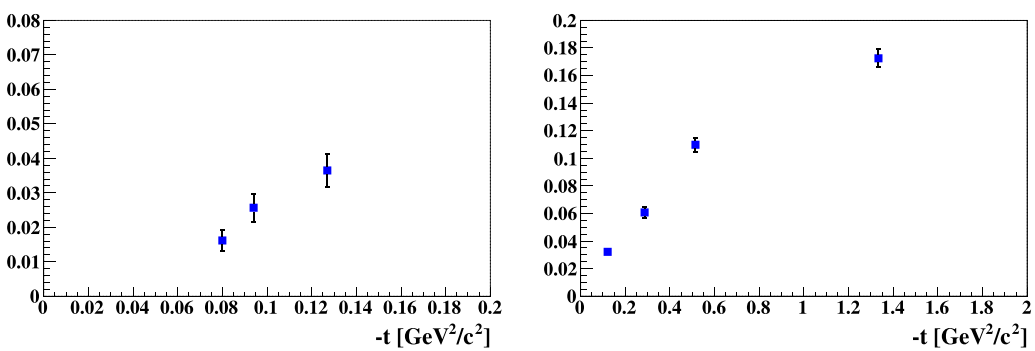


FIG. 16. The estimated coherent (left) and incoherent (right) π^0 contamination fraction in the DVCS events as a function of the transferred momentum squared $-t$ and integrated over the kinematic variables Q^2 , x_B , and ϕ .

TABLE I. The systematic uncertainties on the measured coherent and incoherent BSAs at $\phi = 90$ deg.

Systematic source	Coherent channel	Incoherent channel	Type of systematic error
Beam polarization	3.5%	3.5%	Normalization
DVCS cuts	8%	6%	Bin to bin
Data binning	5.1%	7.1%	Bin to bin
π^0 subtraction	0.6%	2.0%	Bin to bin
Radiative corrections	0.1%	0.1%	Bin to bin
Total bin to bin	10.1%	10.1%	Bin to bin

of the coherent DVCS process from the incoherent background.

We show the extraction of the BSA at 90 degrees in Fig. 19 together with the past HERMES Collaboration results [10]. Two models are compared to the data; they are both based on the hypothesis that the main nuclear effects are included by accounting for the nucleon off-shellness and the kinematics of nucleons in nuclei. The one by Liuti *et al.* [30,31] appears to undershoot the results systematically. However, the more recent and independent calculation by Fucini *et al.* [32], using similar principles but with a nondiagonal nuclear spectral function [33] based on the AV18 nucleon-nucleon potential [34] and the UIV three-body forces [35], has been able to reproduce the data very well. A factor in the difference is that the recent calculation by Fucini *et al.* [32] benefited from using the precise kinematics of each of the points presented in Appendix B. Including this information appears to have a significant impact on some points; for instance the $-t$ distribution appears to have a peculiar structure that is well reproduced when using this information.

One of the motivations for the choice of ${}^4\text{He}$ for the coherent DVCS measurement was a simplified extraction of the CFF \mathcal{H}_A from the data. To perform this step, we used the form from Eq. (6) to fit the data in Fig. 18. We present in Fig. 20 the extracted real and imaginary parts of the single CFF of the ${}^4\text{He}$ nucleus. The results are rather encouraging. The two parts of the CFF are constrained by data without the need for any model assumption. This capacity to obtain a

model-independent result with such a limited data set offers a striking contrast with the situation of the free-proton fits [36,37].

The CFF extraction allows us to compare the results to other theoretical calculations. These are performed within the impulse approximation [18,38] and give the nuclear GPD directly from the proton and neutron GPDs. In Fig. 20, we show two versions of this calculation, where two different nucleon GPD models are used as input, compared with the calculation previously shown by Liuti *et al.* [30] with an updated nucleon model [31]. We can see that the effect of changing the input nucleon GPD model is of similar size or larger than the difference between the nuclear models. However, at the level of precision of the present data, it is not possible to resolve which variant is best. This feature highlights the importance of the choice of nucleon model to study nuclear effects with this data.

In summary, this measurement of the BSA in the deeply virtual coherent exclusive photoproduction on a nucleus is the first to clearly isolate the effect of coherent nuclear DVCS and of nuclear GPDs. While the statistical precision and the kinematic coverage are still behind the experimental results of the proton, the results appear to match very well the predictions using the GPD framework. Moreover, the extraction of the CFF appears to be very convenient based on the BSA measurement only. Together, these findings validate the relevance of coherent nuclear DVCS to study the nucleus globally in terms of quarks and gluons.

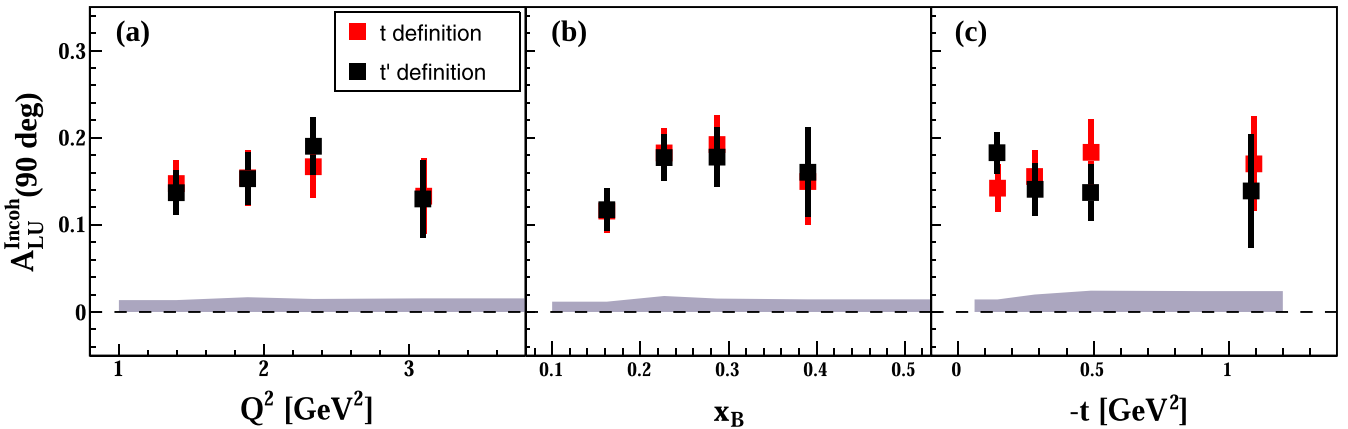


FIG. 17. The BSA at 90 degrees [$A_{LU}^{\text{Incoh}}(90 \text{ deg})$] as a function of Q^2 (a), x_B (b), and $-t$ (c), using the photon-based t definition (red) and the proton-based t' definition (black).

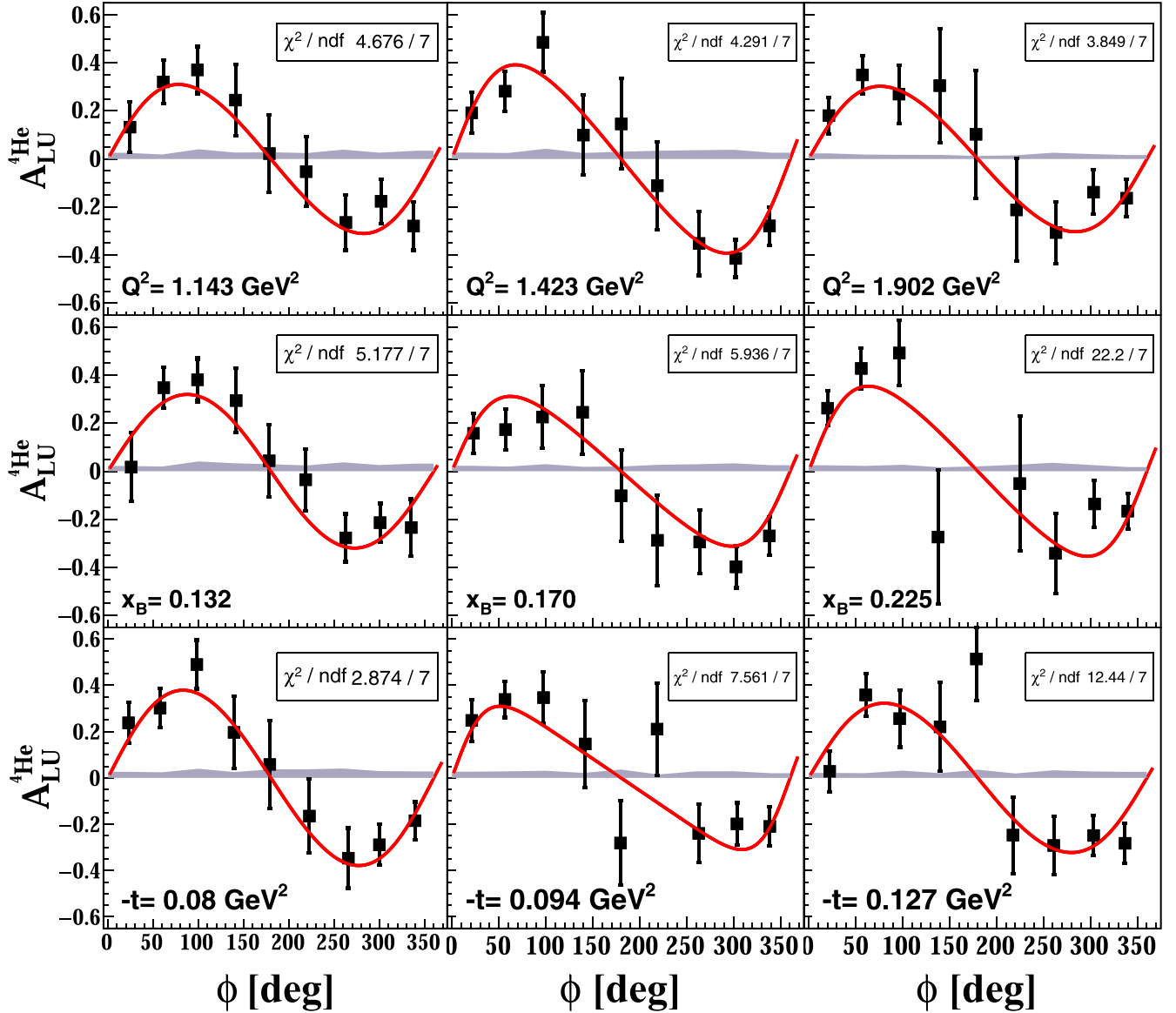


FIG. 18. The BSA in the coherent exclusive photoproduction off ${}^4\text{He}$ as a function of ϕ and Q^2 (top panels), x (middle panels), and $-t$ (lower panels). The error bars are statistical and the gray bands represent the systematic uncertainties. The full red lines show the fit of the data with the form of Eq. (6).

B. Incoherent DVCS

The results for the measurement of the BSA in the incoherent DVCS channel are presented in Fig. 21. They display patterns rather similar to those observed with the free proton, with a clear domination of their sinusoidal component. To compare the data to models, we extract the BSA at 90 degrees with a fit of the form $\frac{\alpha \sin(\phi)}{1+\beta \cos(\phi)}$.

The asymmetries at 90 degrees are presented in Fig. 22 together with the theoretical calculation by the same groups as presented in Fig. 19. We observe a significant improvement on the precision compared to the HERMES data, which offers more constraint on the models presented. As in the coherent case, the calculation appears to have issues reproducing the shape of the data, with Fucini *et al.* [41] doing better than the

others. However, this time the calculations overshoot the data, sometimes by a significant amount.

An interesting way to look into this data is to show the result on incoherent nuclear DVCS compared with the free-proton one. We can for instance make a ratio, in a fashion similar to the EMC effect, which allows us to cancel out the effects from the nucleon structure and highlight nuclear effects. Such a ratio is presented in Fig. 23. Notably, the calculation by Fucini *et al.* [41] appears closer than the others with this observable. This feature indicates that the different raw asymmetry results might be linked to the different input model used for the free-nucleon GPD rather than to differences in the treatment of the nuclear effects. Also, Fucini *et al.* appear to roughly reproduce the shape of the x_B distribution, which might indicate that it is linked to correlations be-

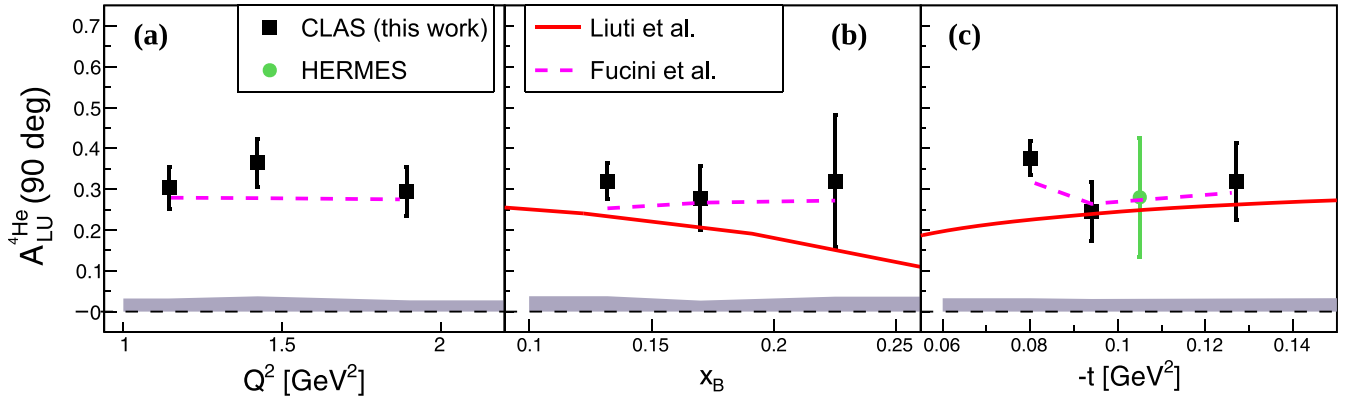


FIG. 19. The BSA at 90 degrees as a function of Q^2 (a), x (b), and $-t$ (c). Our results are shown with black squares, HERMES results with green circles [10]. The theoretical prediction by Liuti *et al.* [30,31] is shown by the full blue line, while the calculation by Fucini *et al.* [32] is shown with the magenta dashed line.

tween kinematic variables. In conclusion, the BSA in the incoherent DVCS channel is suppressed by 20% to 30% compared to the free proton, which was not expected by most models.

The explanation for this surprising behavior can come from different sources both in the initial state and in the final state. Further work is needed to fully comprehend this newly discovered nuclear effect. On the experimental side, the use of tagging methods, where the nuclear fragments are measured, appears to offer the best option forward. Indeed, tagging offers the best chance to understand better this result by offering better control over both the initial- and the final-state effects [2].

VII. SUMMARY

We report the measurement of the coherent and incoherent DVCS processes off ${}^4\text{He}$ with CLAS at JLab. To properly isolate the coherent channel, the experiment used a specially designed RTPC to detect the scattered ${}^4\text{He}$. This coherent DVCS measurement reveals the large BSA ($\sim 35\%$) expected by theoretical calculations made in the impulse approximation. Moreover, we showed that the CFF extraction can be immediately performed using these data without any model assumptions. The incoherent DVCS measurement however reveals relatively small asymmetries in comparison to previ-

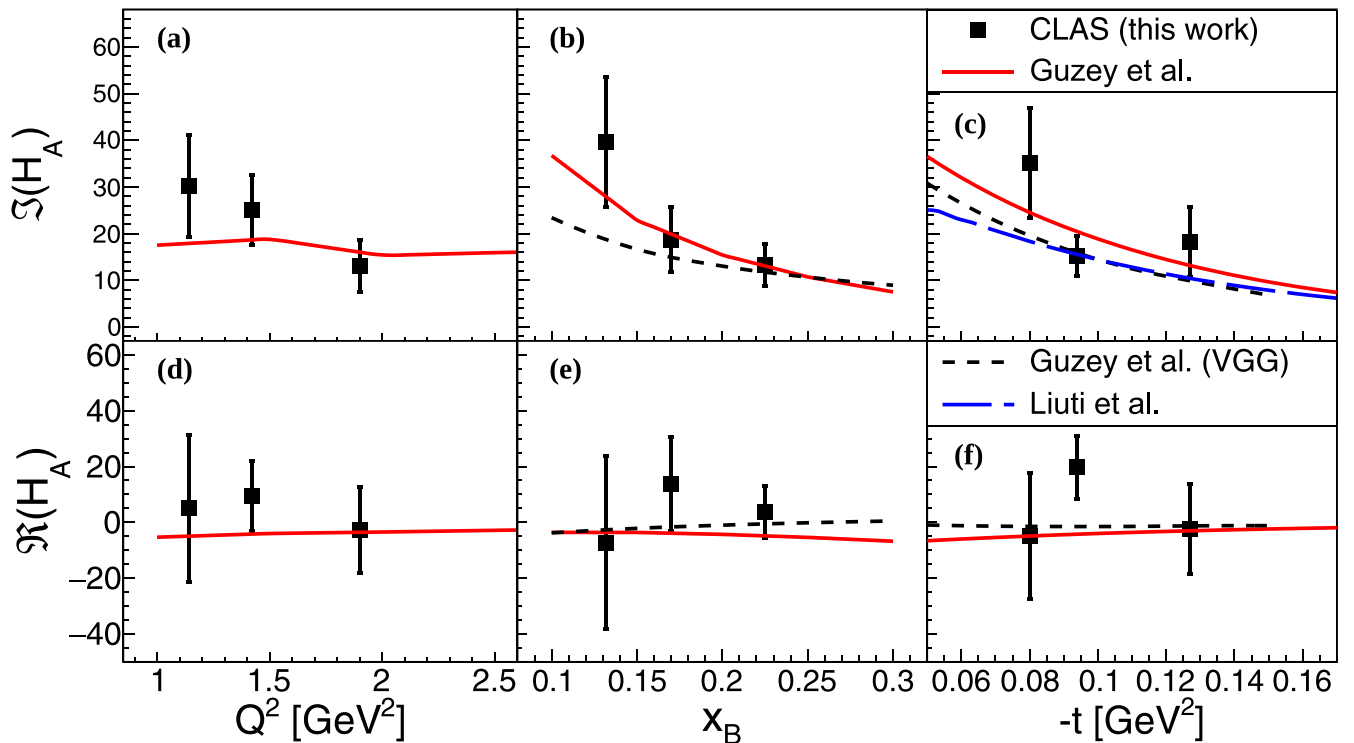


FIG. 20. The imaginary part of the ${}^4\text{He}$ CFF \mathcal{H}_A is shown as a function of Q^2 (a), x (b), and $-t$ (c). The real part of the ${}^4\text{He}$ CFF \mathcal{H}_A is shown as a function of Q^2 (d), x (e), and $-t$ (f). The red full line is the theoretical calculation by Guzey *et al.* [18,38], the black dashed line is the same calculation using the VGG model as input [39,40], and the blue long-dashed line shows the predictions by Liuti *et al.* [30,31].

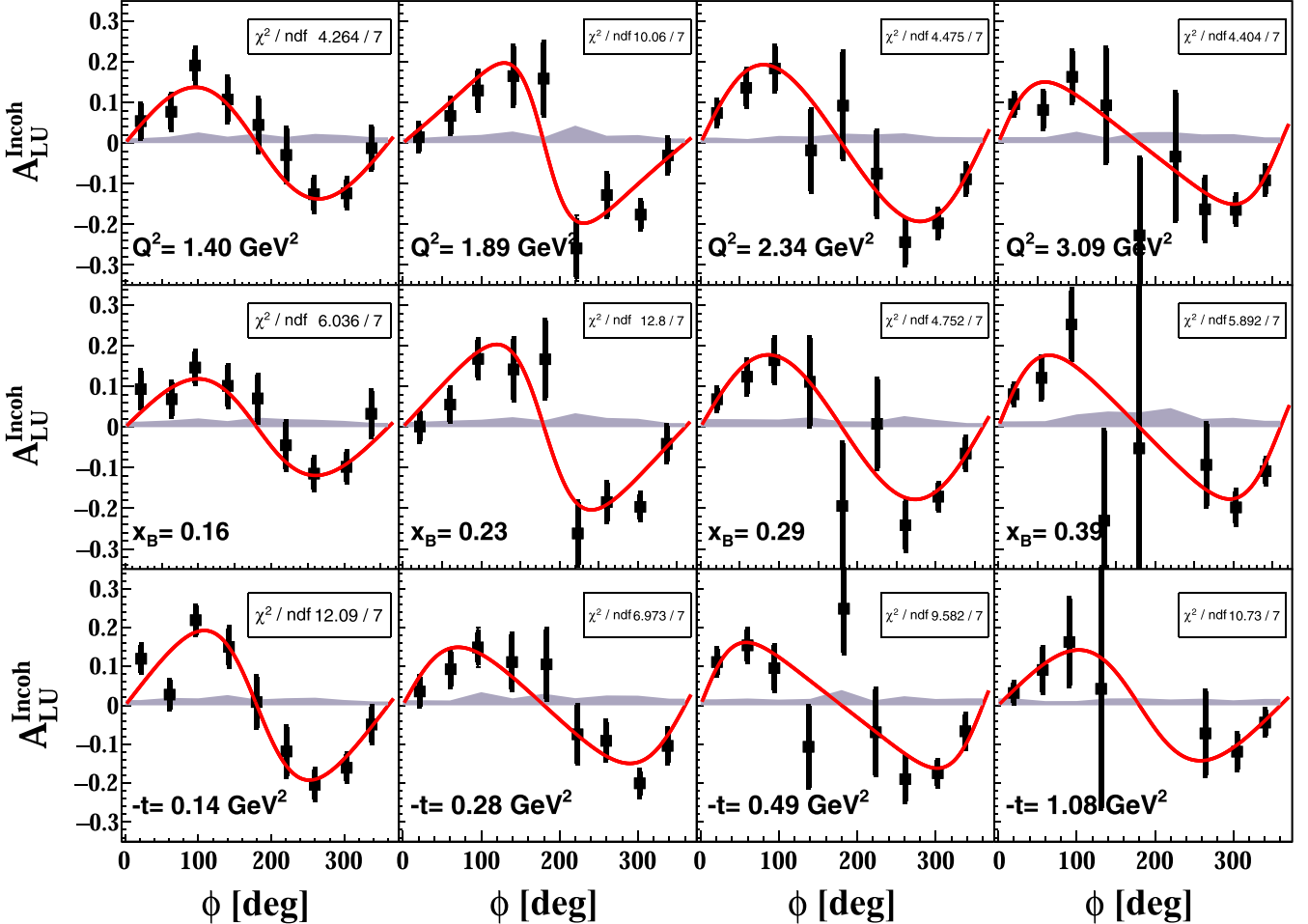


FIG. 21. The BSA in the incoherent exclusive photoproduction off a proton bound in ${}^4\text{He}$ as a function of ϕ and Q^2 (top panels), x (middle panels), and $-t$ (lower panels). The error bars are statistical and the gray bands represent the systematic uncertainties. The data are fitted with the form $\frac{\alpha \sin(\phi)}{1+\beta \cos(\phi)}$; the results of the fits are drawn with black full lines.

ous free-proton measurements. The source of this suppression of the BSA remains unclear as both initial- and final-state effect contributions could lead to such outcome. We presented various models for both channels. While old and recent work agree nicely with the data from the coherent channel, it appears more difficult to reproduce the incoherent DVCS data. A future experimental program using tagging at the upgraded CLAS12 detector with an 11 GeV electron beam is planned to address this question in the coming years by using a new recoil detector design [42].

ACKNOWLEDGMENTS

The authors acknowledge the staff of the Accelerator and Physics Divisions at the Thomas Jefferson National Accelerator Facility who made this experiment possible. This work was supported in part by the Chilean Comisión Nacional de Investigación Científica y Tecnológica (CONICYT), by CONICYT PIA Grant No. ACT1413, the Italian Istituto Nazionale di Fisica Nucleare, the French Centre National de la Recherche Scientifique, the French Commissariat à l'Energie Atomique, the US Department of Energy

under Contract No. DE-AC02-06CH11357, the United Kingdom Science and Technology Facilities Council (STFC), the Scottish Universities Physics Alliance (SUPA), the National Research Foundation of Korea, and the Office of Research and Economic Development at Mississippi State University. M. Hattawy also acknowledges the support of the Consulat Général de France à Jérusalem. This work has received funding from the European Research Council (ERC) under the European Union's Horizon 2020 research and innovation program (Grant Agreement No. 804480). The Southeastern Universities Research Association operates the Thomas Jefferson National Accelerator Facility for the United States Department of Energy under Contract No. DE-AC05-06OR23177.

APPENDIX A: EXPRESSIONS FOR THE BSA OF THE COHERENT DVCS

We present in this Appendix the detailed expressions used for Eq. (5) and Eqs. (7) to (10). These are adapted from the work of Kirchner and Müller [13] to match the notations and conventions used in this work.

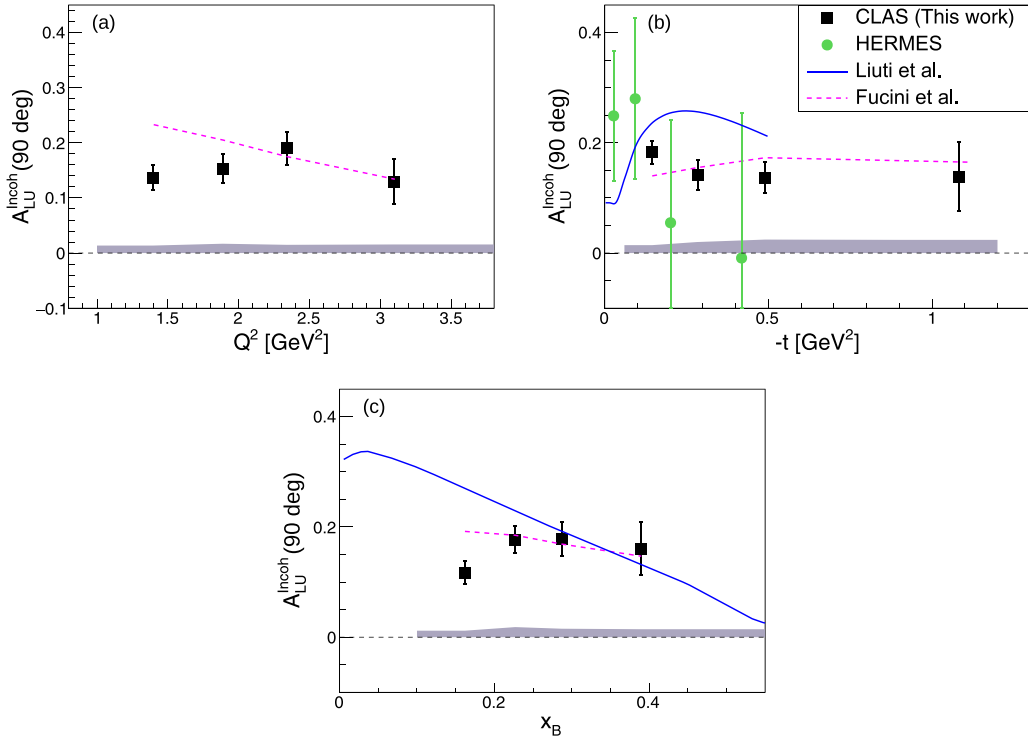


FIG. 22. The BSA at 90 degrees as a function of Q^2 (a), $-t$ (b), and x_B (c). Our measurement is represented with black squares and the HERMES measurement [10] with green circles. The theoretical prediction by Liuti *et al.* [30,31] is shown by the full blue line, while the calculation by Fucini *et al.* [41] is shown with the magenta dashed line.

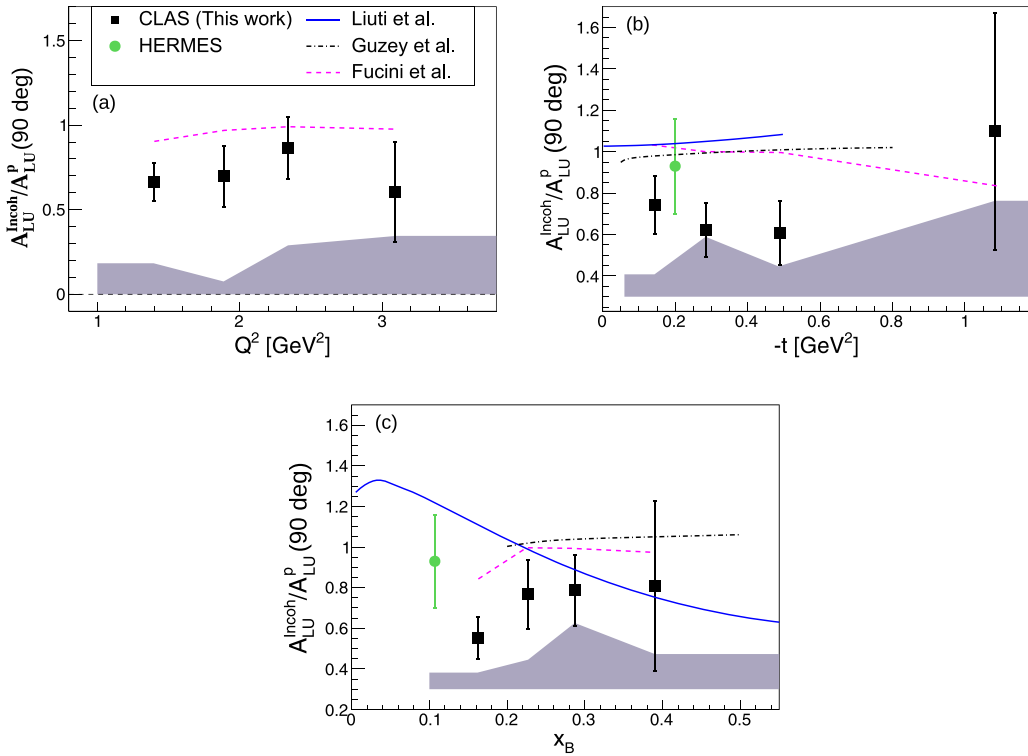


FIG. 23. DVCS BSA ratio of the bound proton to the free proton as a function of Q^2 (a), $-t$ (b), and x_B (c). The present measurement is represented with black squares and the HERMES measurement [10] with green circles. The theoretical prediction by Liuti *et al.* [30,31] is shown by the full blue line, the calculation by Fucini *et al.* [41] is shown with the magenta dashed line, and the black dot-dashed line is the calculation by Guzey *et al.* [38].

First, $\mathcal{P}_1(\phi)$ and $\mathcal{P}_2(\phi)$ are BH propagators and defined as

$$\mathcal{P}_1(\phi) = \frac{(k - q')^2}{Q^2} = -\frac{1}{y(1 + \epsilon^2)}[J + 2K \cos(\phi)], \quad (\text{A1})$$

$$\mathcal{P}_2(\phi) = \frac{(k - \Delta)^2}{Q^2} = 1 + \frac{t}{Q^2} + \frac{1}{y(1 + \epsilon^2)}[J + 2K \cos(\phi)], \quad (\text{A2})$$

with

$$J = \left(1 - y - \frac{y\epsilon^2}{2}\right)\left(1 + \frac{t}{Q^2}\right) - (1 - x_A)(2 - y)\frac{t}{Q^2}, \quad (\text{A3})$$

$$K^2 = -\delta t (1 - x_A)\left(1 - y - \frac{y^2\epsilon^2}{4}\right) \times \left\{\sqrt{1 + \epsilon^2} + \frac{4x_A(1 - x_A) + \epsilon^2}{4(1 - x_A)}\delta t\right\}, \quad (\text{A4})$$

$$\delta t = \frac{t - t_{\min}}{Q^2} = \frac{t}{Q^2} + \frac{2(1 - x_A)(1 - \sqrt{1 + \epsilon^2}) + \epsilon^2}{4x_A(1 - x_A) + \epsilon^2}. \quad (\text{A5})$$

The Fourier coefficients for BH contributions are defined as

$$c_0^{\text{BH}} = \left[\{(2 - y)^2 + y^2(1 + \epsilon^2)^2\}\left\{\frac{\epsilon^2 Q^2}{t} + 4(1 - x_A) + (4x_A + \epsilon^2)\frac{t}{Q^2}\right\} + 2\epsilon^2\{4(1 - y)(3 + 2\epsilon^2) + y^2(2 - \epsilon^4)\} - 4x_A^2(2 - y)^2(2 + \epsilon^2)\frac{t}{Q^2} + 8K^2\frac{\epsilon^2 Q^2}{t}\right]F_A^2(t), \quad (\text{A6})$$

$$c_1^{\text{BH}} = -8(2 - y)K\left\{2x_A + \epsilon^2 - \frac{\epsilon^2 Q^2}{t}\right\}F_A^2(t), \quad (\text{A7})$$

$$c_2^{\text{BH}} = 8K^2\frac{\epsilon^2 Q^2}{t}F_A^2(t), \quad (\text{A8})$$

where $F_A(t)$ is the electromagnetic form factor of ${}^4\text{He}$. The coefficient for the DVCS contribution is given by

$$c_0^{\text{DVCS}} = 2\frac{2 - 2y + y^2 + \frac{\epsilon^2}{2}y^2}{1 + \epsilon^2} \mathcal{H}_A \mathcal{H}_A^*. \quad (\text{A9})$$

Finally, the interference amplitude coefficients are written as

$$s_1^{\text{INT}} = F_A(t)\text{Im}(\mathcal{H}_A)S_{++}(1), \quad (\text{A10})$$

with

$$S_{++}(1) = \frac{-8K(2 - y)y}{1 + \epsilon^2}\left(1 + \frac{1 - x_A + \frac{\sqrt{1 + \epsilon^2} - 1}{2}}{1 + \epsilon^2}\frac{t - t_{\min}}{Q^2}\right), \quad (\text{A11})$$

$$c_0^{\text{INT}} = F_A(t)\text{Re}(\mathcal{H}_A)C_{++}(0), \quad (\text{A12})$$

with

$$C_{++}(0) = \frac{-4(2 - y)(1 + \sqrt{1 + \epsilon^2})}{(1 + \epsilon^2)^2}\left\{\frac{\tilde{K}^2}{Q^2}\frac{(2 - y)^2}{\sqrt{1 + \epsilon^2}} + \frac{t}{Q^2}\left(1 - y - \frac{\epsilon^2}{4}y^2\right)(2 - x_A)\left(1 + \frac{2x_A(2 - x_A + \frac{\sqrt{1 + \epsilon^2} - 1}{2} + \frac{\epsilon^2}{2x_A})\frac{t}{Q^2} + \epsilon^2}{(2 - x_A)(1 + \sqrt{1 + \epsilon^2})}\right)\right\}, \quad (\text{A13})$$

$$c_1^{\text{INT}} = F_A(t)\text{Re}(\mathcal{H}_A)C_{++}(1), \quad (\text{A14})$$

with

$$C_{++}(1) = \frac{-16K(1 - y + \frac{\epsilon^2}{4}y^2)}{(1 + \epsilon^2)^{5/2}}\left\{\left(1 + (1 - x_A)\frac{\sqrt{1 + \epsilon^2} - 1}{2x_A} + \frac{\epsilon^2}{4x_A}\right)\frac{x_A t}{Q^2} - \frac{3\epsilon^2}{4.0}\right\} - 4K\left(2 - 2y + y^2 + \frac{\epsilon^2}{2}y^2\right)\frac{1 + \sqrt{1 + \epsilon^2} - \epsilon^2}{(1 + \epsilon^2)^{5/2}}\left\{1 - (1 - 3x_A)\frac{t}{Q^2} + \frac{1 - \sqrt{1 + \epsilon^2} + 3\epsilon^2}{1 + \sqrt{1 + \epsilon^2} - \epsilon^2}\frac{x_A t}{Q^2}\right\}. \quad (\text{A15})$$

APPENDIX B: TABLES OF RESULTS WITH KINEMATICS INFORMATION

See Tables II–IX for the results and information.

TABLE II. Values of the coherent A_{LU} in Q^2 bins from Fig. 18.

$\langle Q^2 \rangle$ (GeV 2)	$\langle x_B \rangle$	$\langle -t \rangle$ (GeV 2)	$\langle \phi \rangle$ (deg)	$A_{LU} \pm \text{stat.} \pm \text{syst.}$
1.14	0.136	0.096	24	$0.133 \pm 0.109 \pm 0.026$
			61	$0.321 \pm 0.093 \pm 0.019$
			99	$0.371 \pm 0.103 \pm 0.040$
			141	$0.245 \pm 0.152 \pm 0.027$
			178	$0.023 \pm 0.163 \pm 0.028$
			219	$-0.053 \pm 0.148 \pm 0.025$
			263	$-0.264 \pm 0.120 \pm 0.039$
			302	$-0.176 \pm 0.097 \pm 0.026$
			338	$-0.279 \pm 0.105 \pm 0.034$
			21	$0.192 \pm 0.089 \pm 0.027$
			57	$0.282 \pm 0.087 \pm 0.025$
			97	$0.486 \pm 0.129 \pm 0.043$
1.42	0.172	0.099	140	$0.100 \pm 0.168 \pm 0.025$
			180	$0.146 \pm 0.191 \pm 0.030$
			219	$-0.111 \pm 0.185 \pm 0.034$
			263	$-0.352 \pm 0.137 \pm 0.037$
			302	$-0.414 \pm 0.084 \pm 0.038$
			338	$-0.279 \pm 0.084 \pm 0.026$
			21.4	$0.180 \pm 0.081 \pm 0.023$
			57.2	$0.350 \pm 0.082 \pm 0.019$
			96.2	$0.270 \pm 0.123 \pm 0.017$
			139.5	$0.305 \pm 0.239 \pm 0.017$
			178.2	$0.103 \pm 0.267 \pm 0.013$
			221.4	$-0.212 \pm 0.215 \pm 0.015$
1.90	0.224	0.107	263.3	$-0.306 \pm 0.131 \pm 0.026$
			303.3	$-0.138 \pm 0.094 \pm 0.021$
			338.5	$-0.163 \pm 0.079 \pm 0.016$

TABLE III. Values of the coherent A_{LU} in x_B bins from Fig. 18.

$\langle Q^2 \rangle$ (GeV 2)	$\langle x_B \rangle$	$\langle -t \rangle$ (GeV 2)	$\langle \phi \rangle$ (deg)	$A_{LU} \pm \text{stat.} \pm \text{syst.}$
1.16	0.132	0.095	26	$0.017 \pm 0.144 \pm 0.022$
			62	$0.348 \pm 0.087 \pm 0.020$
			99	$0.381 \pm 0.095 \pm 0.041$
			142	$0.294 \pm 0.138 \pm 0.033$
			178	$0.043 \pm 0.152 \pm 0.029$
			219	$-0.035 \pm 0.132 \pm 0.024$
			263	$-0.277 \pm 0.105 \pm 0.037$
			301	$-0.214 \pm 0.084 \pm 0.026$
			335	$-0.234 \pm 0.122 \pm 0.032$
			23	$0.158 \pm 0.085 \pm 0.023$
			57	$0.173 \pm 0.088 \pm 0.020$
			96	$0.226 \pm 0.133 \pm 0.030$
			139	$0.245 \pm 0.176 \pm 0.019$
1.44	0.170	0.099	180	$-0.102 \pm 0.192 \pm 0.020$
			219	$-0.288 \pm 0.191 \pm 0.027$
			264	$-0.294 \pm 0.136 \pm 0.029$
			303	$-0.398 \pm 0.092 \pm 0.033$
			338	$-0.269 \pm 0.083 \pm 0.025$
			20	$0.263 \pm 0.076 \pm 0.025$
			56	$0.428 \pm 0.089 \pm 0.022$
			96	$0.493 \pm 0.139 \pm 0.027$
			138	$-0.274 \pm 0.280 \pm 0.017$
			180	$0.847 \pm 0.250 \pm 0.020$
			225	$-0.051 \pm 0.281 \pm 0.027$
			263	$-0.342 \pm 0.169 \pm 0.035$
			305	$-0.136 \pm 0.103 \pm 0.026$
			340	$-0.166 \pm 0.077 \pm 0.018$

TABLE IV. Values of the coherent A_{LU} in $-t$ bins from Fig. 18.

$\langle Q^2 \rangle$ (GeV 2)	$\langle x_B \rangle$	$\langle -t \rangle$ (GeV 2)	$\langle \phi \rangle$ (deg)	$A_{LU} \pm \text{stat.} \pm \text{syst.}$
1.36	0.160	0.080	23	$0.238 \pm 0.093 \pm 0.026$
			58	$0.301 \pm 0.087 \pm 0.024$
			98	$0.490 \pm 0.112 \pm 0.039$
			139	$0.197 \pm 0.160 \pm 0.025$
			179	$0.058 \pm 0.192 \pm 0.037$
			223	$-0.165 \pm 0.164 \pm 0.037$
			266	$-0.347 \pm 0.134 \pm 0.040$
			300	$-0.289 \pm 0.093 \pm 0.029$
			339	$-0.185 \pm 0.086 \pm 0.028$
			21	$0.248 \pm 0.093 \pm 0.027$
1.51	0.179	0.094	56	$0.339 \pm 0.083 \pm 0.028$
			98	$0.347 \pm 0.116 \pm 0.031$
			142	$0.146 \pm 0.189 \pm 0.022$
			180	$-0.281 \pm 0.186 \pm 0.036$
			219	$0.210 \pm 0.200 \pm 0.015$
			263	$-0.240 \pm 0.128 \pm 0.028$
			304	$-0.199 \pm 0.096 \pm 0.029$
			339	$-0.210 \pm 0.088 \pm 0.020$
			22	$0.028 \pm 0.091 \pm 0.021$
			61	$0.358 \pm 0.093 \pm 0.020$
1.61	0.193	0.127	97	$0.256 \pm 0.127 \pm 0.031$
			140	$0.221 \pm 0.193 \pm 0.020$
			179	$0.514 \pm 0.183 \pm 0.035$
			218	$-0.247 \pm 0.166 \pm 0.019$
			261	$-0.292 \pm 0.130 \pm 0.033$
			303	$-0.249 \pm 0.089 \pm 0.028$
			337	$-0.283 \pm 0.090 \pm 0.026$

TABLE V. Values of the incoherent A_{LU} in Q^2 bins from Fig. 21.

$\langle Q^2 \rangle$ (GeV 2)	$\langle x_B \rangle$	$\langle -t \rangle$ (GeV 2)	$\langle \phi \rangle$ (deg)	$A_{LU} \pm \text{stat.} \pm \text{syst.}$
1.40	0.166	0.376	21	$0.054 \pm 0.044 \pm 0.012$
			63	$0.077 \pm 0.046 \pm 0.016$
			95	$0.191 \pm 0.047 \pm 0.026$
			140	$0.108 \pm 0.056 \pm 0.016$
			182	$0.045 \pm 0.069 \pm 0.023$
			220	$-0.029 \pm 0.068 \pm 0.015$
			258	$-0.126 \pm 0.046 \pm 0.023$
			303	$-0.124 \pm 0.040 \pm 0.020$
			337	$-0.012 \pm 0.054 \pm 0.014$
			20	$0.014 \pm 0.036 \pm 0.012$
			61	$0.067 \pm 0.046 \pm 0.017$
			96	$0.130 \pm 0.052 \pm 0.020$
			141	$0.165 \pm 0.077 \pm 0.029$
			180	$0.159 \pm 0.089 \pm 0.015$
1.89	0.232	0.415	222	$-0.259 \pm 0.081 \pm 0.043$
			260	$-0.128 \pm 0.056 \pm 0.018$
			304	$-0.176 \pm 0.039 \pm 0.020$
			338	$-0.030 \pm 0.045 \pm 0.011$
			21	$0.074 \pm 0.033 \pm 0.014$
			58	$0.136 \pm 0.046 \pm 0.010$
			95	$0.184 \pm 0.057 \pm 0.018$
			141	$-0.018 \pm 0.101 \pm 0.016$
			182	$0.092 \pm 0.133 \pm 0.024$
			225	$-0.075 \pm 0.107 \pm 0.021$
			261	$-0.244 \pm 0.060 \pm 0.024$
			303	$-0.198 \pm 0.038 \pm 0.015$
			339	$-0.089 \pm 0.040 \pm 0.015$
2.34	0.288	0.497	20	$0.096 \pm 0.030 \pm 0.015$
			57	$0.082 \pm 0.048 \pm 0.015$
			94	$0.163 \pm 0.069 \pm 0.028$
			138	$0.093 \pm 0.141 \pm 0.013$
			180	$-0.227 \pm 0.192 \pm 0.027$
			226	$-0.033 \pm 0.160 \pm 0.027$
			264	$-0.163 \pm 0.080 \pm 0.021$
			303	$-0.164 \pm 0.041 \pm 0.022$
			341	$-0.091 \pm 0.037 \pm 0.014$

TABLE VI. Values of the incoherent A_{LU} in x_B bins from Fig. 21.

$\langle Q^2 \rangle$ (GeV 2)	$\langle x_B \rangle$	$\langle -t \rangle$ (GeV 2)	$\langle \phi \rangle$ (deg)	$A_{LU} \pm \text{stat.} \pm \text{syst.}$
1.45	0.163	0.374	21	$0.094 \pm 0.046 \pm 0.014$
			63	$0.069 \pm 0.044 \pm 0.017$
			96	$0.147 \pm 0.044 \pm 0.022$
			140	$0.102 \pm 0.052 \pm 0.015$
			181	$0.071 \pm 0.062 \pm 0.024$
			220	$-0.045 \pm 0.062 \pm 0.020$
			259	$-0.115 \pm 0.043 \pm 0.018$
			303	$-0.098 \pm 0.039 \pm 0.015$
			337	$0.033 \pm 0.057 \pm 0.011$
			22	$0.002 \pm 0.038 \pm 0.013$
			60	$0.056 \pm 0.044 \pm 0.016$
			96	$0.168 \pm 0.050 \pm 0.018$
			141	$0.142 \pm 0.079 \pm 0.025$
			182	$0.167 \pm 0.096 \pm 0.017$
			223	$-0.262 \pm 0.083 \pm 0.034$
1.93	0.225	0.381	260	$-0.185 \pm 0.052 \pm 0.023$
			303	$-0.196 \pm 0.037 \pm 0.021$
			337	$-0.041 \pm 0.046 \pm 0.010$
			21	$0.069 \pm 0.033 \pm 0.020$
			59	$0.124 \pm 0.046 \pm 0.020$
			94	$0.165 \pm 0.058 \pm 0.019$
			139	$0.111 \pm 0.110 \pm 0.024$
			181	$-0.194 \pm 0.155 \pm 0.015$
			225	$0.008 \pm 0.111 \pm 0.014$
			261	$-0.242 \pm 0.066 \pm 0.027$
			303	$-0.171 \pm 0.038 \pm 0.018$
			338	$-0.065 \pm 0.041 \pm 0.010$
			20	$0.081 \pm 0.029 \pm 0.014$
			55	$0.121 \pm 0.054 \pm 0.015$
			93	$0.253 \pm 0.090 \pm 0.031$
2.98	0.389	0.688	135	$-0.230 \pm 0.225 \pm 0.039$
			180	$-0.052 \pm 0.425 \pm 0.036$
			231	$-0.377 \pm 0.334 \pm 0.047$
			266	$-0.093 \pm 0.103 \pm 0.020$
			303	$-0.198 \pm 0.045 \pm 0.023$
			341	$-0.108 \pm 0.035 \pm 0.016$

TABLE VII. Values of the incoherent A_{LU} in $-t$ bins from Fig. 21.

$\langle Q^2 \rangle$ (GeV 2)	$\langle x_B \rangle$	$\langle -t \rangle$ (GeV 2)	$\langle \phi \rangle$ (deg)	$A_{LU} \pm \text{stat.} \pm \text{syst.}$
1.84	0.215	0.135	22	$0.120 \pm 0.037 \pm 0.014$
			61	$0.027 \pm 0.042 \pm 0.019$
			96	$0.219 \pm 0.041 \pm 0.018$
			142	$0.150 \pm 0.054 \pm 0.026$
			180	$0.008 \pm 0.067 \pm 0.015$
			221	$-0.119 \pm 0.065 \pm 0.018$
			260	$-0.204 \pm 0.043 \pm 0.020$
			303	$-0.160 \pm 0.037 \pm 0.014$
			338	$-0.049 \pm 0.047 \pm 0.010$
			21	$0.036 \pm 0.040 \pm 0.013$
			61	$0.093 \pm 0.045 \pm 0.013$
			96	$0.149 \pm 0.051 \pm 0.034$
			139	$0.111 \pm 0.073 \pm 0.018$
2.15	0.257	0.281	183	$0.105 \pm 0.093 \pm 0.030$
			223	$-0.074 \pm 0.076 \pm 0.018$
			259	$-0.091 \pm 0.055 \pm 0.025$
			302	$-0.200 \pm 0.039 \pm 0.025$
			338	$-0.104 \pm 0.047 \pm 0.017$
			21	$0.111 \pm 0.037 \pm 0.015$
			60	$0.154 \pm 0.045 \pm 0.018$
			94	$0.096 \pm 0.060 \pm 0.015$
			138	$-0.107 \pm 0.105 \pm 0.017$
			183	$0.248 \pm 0.119 \pm 0.039$
			224	$-0.069 \pm 0.110 \pm 0.013$
			261	$-0.190 \pm 0.062 \pm 0.023$
			303	$-0.174 \pm 0.036 \pm 0.016$
2.37	0.291	0.492	338	$-0.067 \pm 0.047 \pm 0.018$
			20	$0.032 \pm 0.030 \pm 0.018$
			57	$0.091 \pm 0.058 \pm 0.011$
			91	$0.163 \pm 0.112 \pm 0.011$
			131	$0.042 \pm 0.307 \pm 0.018$
			175	$-0.936 \pm 0.397 \pm 0.018$
			231	$-1.189 \pm 0.517 \pm 0.015$
			264	$-0.072 \pm 0.109 \pm 0.017$
			305	$-0.119 \pm 0.048 \pm 0.013$
			341	$-0.044 \pm 0.036 \pm 0.016$

TABLE VIII. Values of the coherent $A_{LU}(90 \text{ deg})$ in Q^2 (top block), x_B (middle block), and $-t$ (bottom block) bins.

$\langle Q^2 \rangle$ (GeV 2)	$\langle x_B \rangle$	$\langle -t \rangle$ (GeV 2)	$A_{LU}(90 \text{ deg}) \pm \text{stat.} \pm \text{syst.}$
1.14	0.136	0.096	$0.304 \pm 0.051 \pm 0.032$
1.42	0.172	0.099	$0.364 \pm 0.059 \pm 0.037$
1.90	0.224	0.107	$0.295 \pm 0.061 \pm 0.028$
1.16	0.132	0.095	$0.320 \pm 0.045 \pm 0.038$
1.44	0.17	0.099	$0.278 \pm 0.079 \pm 0.027$
1.84	0.225	0.107	$0.320 \pm 0.161 \pm 0.037$
1.36	0.160	0.080	$0.376 \pm 0.042 \pm 0.033$
1.51	0.179	0.094	$0.245 \pm 0.072 \pm 0.031$
1.61	0.193	0.127	$0.318 \pm 0.095 \pm 0.035$

TABLE IX. Values of the incoherent $A_{LU}(90 \text{ deg})$ in Q^2 (top block), x_B (middle block), and $-t$ (bottom block) bins.

$\langle Q^2 \rangle$ (GeV 2)	$\langle x_B \rangle$	$\langle -t \rangle$ (GeV 2)	$A_{LU}(90 \text{ deg}) \pm \text{stat.} \pm \text{syst.}$
1.40	0.166	0.376	$0.137 \pm 0.022 \pm 0.014$
1.89	0.232	0.415	$0.153 \pm 0.027 \pm 0.017$
2.34	0.288	0.497	$0.190 \pm 0.030 \pm 0.017$
3.10	0.379	0.641	$0.130 \pm 0.041 \pm 0.016$
1.45	0.163	0.374	$0.117 \pm 0.021 \pm 0.012$
1.93	0.225	0.381	$0.177 \pm 0.024 \pm 0.018$
2.33	0.283	0.468	$0.178 \pm 0.031 \pm 0.015$
2.98	0.389	0.688	$0.160 \pm 0.048 \pm 0.014$
1.84	0.215	0.135	$0.183 \pm 0.021 \pm 0.014$
2.15	0.257	0.281	$0.141 \pm 0.027 \pm 0.020$
2.37	0.291	0.492	$0.137 \pm 0.029 \pm 0.024$
2.45	0.312	1.089	$0.139 \pm 0.062 \pm 0.024$

- [1] M. Anselmino, M. Guidal, P. Rossi *et al.*, Topical issue on the 3-D structure of the nucleon, *Eur. Phys. J. A* **52**, 164 (2016).
- [2] R. Dupré and S. Scopetta, 3D structure and nuclear targets, *Eur. Phys. J. A* **52**, 159 (2016).
- [3] P. R. Norton, The EMC effect, *Rep. Prog. Phys.* **66**, 1253 (2003).
- [4] S. Malace, D. Gaskell, D. W. Higinbotham, and I. Cloet, The challenge of the EMC effect: Existing data and future directions, *Int. J. Mod. Phys. E* **23**, 1430013 (2014).
- [5] O. Hen, G. A. Miller, E. Piasetzky, and L. B. Weinstein, Nucleon-nucleon correlations, short-lived excitations, and the quarks within, *Rev. Mod. Phys.* **89**, 045002 (2017).
- [6] M. Diehl, Generalized parton distributions, *Phys. Rep.* **388**, 41 (2003).
- [7] A. V. Belitsky and A. V. Radyushkin, Unraveling hadron structure with generalized parton distributions, *Phys. Rep.* **418**, 1 (2005).
- [8] S. Boffi and B. Pasquini, Generalized parton distributions and the structure of the nucleon, *Riv. Nuovo Cimento* **30**, 387 (2007).
- [9] M. Guidal, H. Moutarde, and M. Vanderhaeghen, Generalized parton distributions in the valence region from deeply virtual Compton scattering, *Rep. Prog. Phys.* **76**, 066202 (2013).
- [10] A. Airapetian *et al.*, Nuclear-mass dependence of azimuthal beam-helicity and beam-charge asymmetries in deeply virtual Compton scattering, *Phys. Rev. C* **81**, 035202 (2010).
- [11] M. Hattawy *et al.*, First Exclusive Measurement of Deeply Virtual Compton Scattering off ${}^4\text{He}$: Toward the 3D Tomography of Nuclei, *Phys. Rev. Lett.* **119**, 202004 (2017).
- [12] M. Hattawy *et al.*, Deeply Virtual Compton Scattering Measurement off Bound Protons, *Phys. Rev. Lett.* **123**, 032502 (2019).
- [13] A. Kirchner and D. Müller, Deeply virtual Compton scattering off nuclei, *Eur. Phys. J. C* **32**, 347 (2003).
- [14] A. V. Belitsky and D. Müller, Refined analysis of photon leptoproduction off spinless target, *Phys. Rev. D* **79**, 014017 (2009).
- [15] V. M. Braun, A. N. Manashov, and B. Pirnay, Finite- t and target mass corrections to DVCS on a scalar target, *Phys. Rev. D* **86**, 014003 (2012).
- [16] W. Cosyn and M. Sargsian, Nuclear final-state interactions in deep inelastic scattering off the lightest nuclei, *Int. J. Mod. Phys. E* **26**, 1730004 (2017).
- [17] J. J. Ethier, N. Doshi, S. Malace, and W. Melnitchouk, Quasielastic electron-deuteron scattering in the weak-binding approximation, *Phys. Rev. C* **89**, 065203 (2014).
- [18] V. Guzey and M. Strikman, DVCS on spinless nuclear targets in impulse approximation, *Phys. Rev. C* **68**, 015204 (2003).
- [19] B. A. Mecking *et al.*, The CEBAF Large Acceptance Spectrometer (CLAS), *Nucl. Instrum. Methods Phys. Res., Sect. A* **503**, 513 (2003).
- [20] M. D. Mestayer *et al.*, The CLAS drift chamber system, *Nucl. Instrum. Methods Phys. Res., Sect. A* **449**, 81 (2000).
- [21] E. S. Smith *et al.*, The time-of-flight system for CLAS, *Nucl. Instrum. Methods Phys. Res., Sect. A* **432**, 265 (1999).
- [22] G. Adams *et al.*, The CLAS Cherenkov detector, *Nucl. Instrum. Methods Phys. Res., Sect. A* **465**, 414 (2001).
- [23] M. Amarian *et al.*, The CLAS forward electromagnetic calorimeter, *Nucl. Instrum. Methods Phys. Res., Sect. A* **460**, 239 (2001).
- [24] E. Seder *et al.*, Longitudinal Target-Spin Asymmetries for Deeply Virtual Compton Scattering, *Phys. Rev. Lett.* **114**, 032001 (2015); Publisher's Note: Longitudinal Target-Spin Asymmetries for Deeply Virtual Compton Scattering, **114**, 089901 (2015).
- [25] H. S. Jo *et al.*, Cross Sections for the Exclusive Photon Electroproduction on the Proton and Generalized Parton Distributions, *Phys. Rev. Lett.* **115**, 212003 (2015).
- [26] N. Hirlinger Saylor *et al.*, Measurement of unpolarized and polarized cross sections for deeply virtual Compton scattering on the proton at Jefferson Laboratory with CLAS, *Phys. Rev. C* **98**, 045203 (2018).
- [27] H. C. Fenker *et al.*, BoNuS: Development and use of a radial TPC using cylindrical GEMs, *Nucl. Instrum. Methods Phys. Res., Sect. A* **592**, 273 (2008).
- [28] N. Baillie *et al.*, Measurement of the Neutron F_2 Structure Function via Spectator Tagging with CLAS, *Phys. Rev. Lett.* **108**, 142001 (2012); Publisher's Note: Measurement of the Neutron F_2 Structure Function via Spectator Tagging with CLAS, **108**, 199902 (2012).
- [29] R. Dupré *et al.*, A radial time projection chamber for α detection in CLAS at JLab, *Nucl. Instrum. Methods Phys. Res., Sect. A* **898**, 90 (2018).
- [30] S. Liuti and S. K. Taneja, Microscopic description of deeply virtual Compton scattering off spin-0 nuclei, *Phys. Rev. C* **72**, 032201(R) (2005).
- [31] J. O. Gonzalez-Hernandez, S. Liuti, G. R. Goldstein, and K. Kathuria, Interpretation of the flavor dependence of nucleon form factors in a generalized parton distribution model, *Phys. Rev. C* **88**, 065206 (2013).
- [32] S. Fucini, S. Scopetta, and M. Viviani, Coherent deeply virtual Compton scattering off ${}^4\text{He}$, *Phys. Rev. C* **98**, 015203 (2018).
- [33] M. Viviani, A. Kievsky, and A. Rinat, GRS computation of deep inelastic electron scattering on ${}^4\text{He}$, *Phys. Rev. C* **67**, 034003 (2003).
- [34] R. B. Wiringa, V. G. J. Stoks, and R. Schiavilla, An accurate nucleon-nucleon potential with charge independence breaking, *Phys. Rev. C* **51**, 38 (1995).
- [35] B. S. Pudliner, V. R. Pandharipande, J. Carlson, and R. B. Wiringa, Quantum Monte Carlo Calculations of $A \leq 6$ Nuclei, *Phys. Rev. Lett.* **74**, 4396 (1995).
- [36] R. Dupré, M. Guidal, and M. Vanderhaeghen, Tomographic image of the proton, *Phys. Rev. D* **95**, 011501(R) (2017).
- [37] R. Dupré, M. Guidal, S. Niccolai, and M. Vanderhaeghen, Analysis of deeply virtual Compton scattering data at Jefferson Lab and proton tomography, *Eur. Phys. J. A* **53**, 171 (2017).
- [38] V. Guzey, Neutron contribution to nuclear DVCS asymmetries, *Phys. Rev. C* **78**, 025211 (2008).
- [39] M. Vanderhaeghen, P. A. M. Guichon, and M. Guidal, Deeply virtual electroproduction of photons and mesons on the nucleon: Leading order amplitudes and power corrections, *Phys. Rev. D* **60**, 094017 (1999).
- [40] M. Guidal, M. V. Polyakov, A. V. Radyushkin, and M. Vanderhaeghen, Nucleon form factors from generalized parton distributions, *Phys. Rev. D* **72**, 054013 (2005).
- [41] S. Fucini, S. Scopetta, and M. Viviani, Catching a glimpse of the parton structure of the bound proton, *Phys. Rev. D* **101**, 071501(R) (2020).
- [42] W. R. Armstrong *et al.*, Spectator-tagged deeply virtual Compton scattering on light nuclei, A proposal to PAC 45 meeting, July 10–14, 2017.